GOMBE GROUP AND PLIOCENE SHIELD VOLCANISM IN TURKANA: INSIGHTS INTO THE RELATIONSHIP BETWEEN MAGMATISM AND STRAIN

By

Sahira M. Cancel Vazquez

A THESIS

Submitted to
Michigan State University
in partial fulfillment of the requirements
for the degree of

Geological Sciences – Master of Science

2022

ABSTRACT

The magma-rich East African Rift System (EARS) is a modern rift zone that provides an opportunity to constrain the existing relationship between magmatism and strain in continental rifts. Within the EARS, the broadly rifted Turkana Depression has been identified as an important locus of strain. This study focused on the magmatic events in the Turkana Depression that began in the Pliocene (ca. 4 Ma) as part of a pulse of basaltic activity known as the Stratoid Phase – the last pulse of basaltic magmatism before strain was accommodated in the axial region of the Turkana Basin. This basaltic pulse began with the eruption of the widespread Gombe Stratoid Series and is followed by less voluminous basaltic activity in the form of shield volcanoes emplaced on top of the Gombe lava flows. We find that the Gombe Stratoid Series is representative of a high flux event with a complex magma plumbing system that was produced by large degrees of decompression melting of the upper mantle during a broad stretching event in Turkana. In contrast, the waning of magma flux resulted in the development of shield volcanoes subsequent to the eruption of the Gombe Stratoid Series. The timing of magmatic activity of some of the shield volcanoes suggests that there was a migration of magmatism towards Lake Turkana. Unlike the Gombe Stratoid Series lavas, we find that shield-volcano lavas require a component derived from metasomatized enriched lithospheric mantle. The contribution of this enriched component is more pronounced towards the east, coincident with a younging of magmatism in this direction. We suggest that the presence of easily fusible material in the continental lithospheric mantle in the vicinity of the Lake Turkana Basin may result in the generation of localized lithospheric melt following the broad plate stretching event that yielded the Gombe Stratoid Series. Lithospheric melts will promote the focusing of formerly broadly distributed plate stretching into a more localized region where plate melting may have occurred. We suggest that melting of enriched lithospheric mantle may account for the modern localization of strain and migration of magmatism and rifting towards the currently active volcanic centers in Lake Turkana Basin.

ACKNOWLEDGEMENTS

This research was conducted as part of the NSF Award #1850606: Assessing the relationship between strain localization and magmatism during rift evolution. I would also like to thank current and former members of my research group for their help and support throughout my Master's degree.

TABLE OF CONTENTS

1. Introduction

Continental rifts are extensive, narrow extensional features typified by rift valleys and sedimentary basins, which eventually transition to seafloor spreading after continental breakup (e.g., Scholz and Contreras, 1998; Ebinger et al., 2013; Keir et al., 2013). Continental rifts are bounded by normal faults at one or both sides, are generally asymmetric, and their widths and segmentation along axes are dependent on the region in which they formed (e.g., Scholz and Contreras, 1998). Normal faulting in continental rift zones thins the brittle crust, which when combined with ductile stretching at deeper lithospheric levels, results in plate stretching and thinning (Ebinger et al., 2013). Continental rifts are zones of lithospheric extension – a response to far-field tectonic stresses, or to heat produced by an ascending mantle plume at the base of the lithosphere (e.g., Ebinger et al., 2013; Merle, 2011). Thus, continental breakup results from changes in the rheology and structure of the lithosphere by heating, deformation, and magmatism (e.g., Keir et al., 2013).

In proposed models of rift evolution, where crustal transformation initially occurs by mechanical extension (e.g., Keir et al., 2013) and later through dilation by focused basaltic activity (e.g., Bridges et al., 2012; Ferguson et al., 2013), the importance of magmatism is evident. However, the relationship between strain localization and magmatic activity in these zones remains ambiguous (e.g., Ebinger, 2005; Keir et al., 2013; Rooney, 2020a). Other poorly constrained factors include the role of the mantle properties (i.e., its chemical, physical, and thermal structures) in melting of upwelling mantle leading to magma intruded in the plate, as well as eruption at the surface (e.g., Shillington et al., 2009). Keir (2014) reasoned that these factors are poorly constrained due to the limitations associated with using passive rifted margins to understand the process of continental breakup. Most rifted margins are tectonically inactive having ruptured more than 100 Ma ago, meaning direct observations of the extensional processes cannot be conducted (Keir, 2014). To understand rift evolution, it is therefore important to study currently active zones of rifting, where tectonic and magmatic processes can be directly addressed (e.g., Keir et al., 2013).

The East African Rift System (EARS) is the archetypal example of an active continental rift (e.g., Ebinger, 2005; Rooney, 2020a). The EARS is comprised of two main branches: the Eastern branch and the

Western branch (Figure 1) (Chorowicz, 2005; Rooney, 2020a). The Eastern branch is a 2200 km long feature that begins in Afar in the north and terminates in the Northern Tanzania Divergence in the south, whereas the Western branch runs through Lake Albert in the north to Lake Malawi in the south, covering a distance of 2100 km (Chorowicz, 2005). Magmatic activity within the EARS began ca. 45 Ma and is still ongoing (e.g., Rooney, 2017; Rooney, 2020a). Initial Cenozoic magmatism (ca. 45-22 Ma) is characterized by flood basalt volcanism, which has been suggested by Rooney (2017) to be a product of the interaction between lithospheric extension and material upwelling from the African Large Low Shear Velocity Province (LLSVP). These flood basalt events were followed by more rift-centered magmatism, which is largely controlled by lithospheric thinning and associated decompression melting of plume-contaminated asthenosphere (e.g., Rooney, 2017). Although it is clear that there exists a relationship between magmatism and extension within continental rifting environments, determining the details of this relationship remain an area of fruitful study (e.g., Muirhead et al., 2022; Rooney et al., 2022).

Within the EARS, the Turkana Depression has been recognized as an important locus of strain throughout the development of the rift (e.g., Bonini et al., 2005; Macgregor, 2015; Purcell, 2018, Rooney, 2020a). Episodic pulses of extension in this region have been accompanied by voluminous basaltic eruptions during the Mid Miocene and also Pliocene (the focus of this work) (Rooney, 2020a). Modern magmatism in the Turkana Depression has become more spatially limited and is now focused in axial magmatic zones of focused intrusion in the Lake Turkana Basin (e.g., Rooney, 2020a; Muirhead et al., 2022). This study focuses on Pliocene magmatism recorded in the Turkana Depression, characterized by an initial widespread basaltic event – the Gombe Stratoid Series – that was followed by basaltic activity in the form of shield volcanoes (Rooney, 2020a, Figure 2). These events provide an excellent opportunity to constrain the conditions that drive widespread magmatism during this time, as well as determining how widespread activity gives way to zones of focused intrusion. Using major and trace element geochemistry and petrographic constraints, we investigate the conditions of melt generation of the Gombe Stratoid Series and Pliocene shield volcanism, as well as the magmatic differentiation of the Gombe Stratoid Series. We find that the Gombe Stratoid Series shares significant characteristics with previous flood basalt events

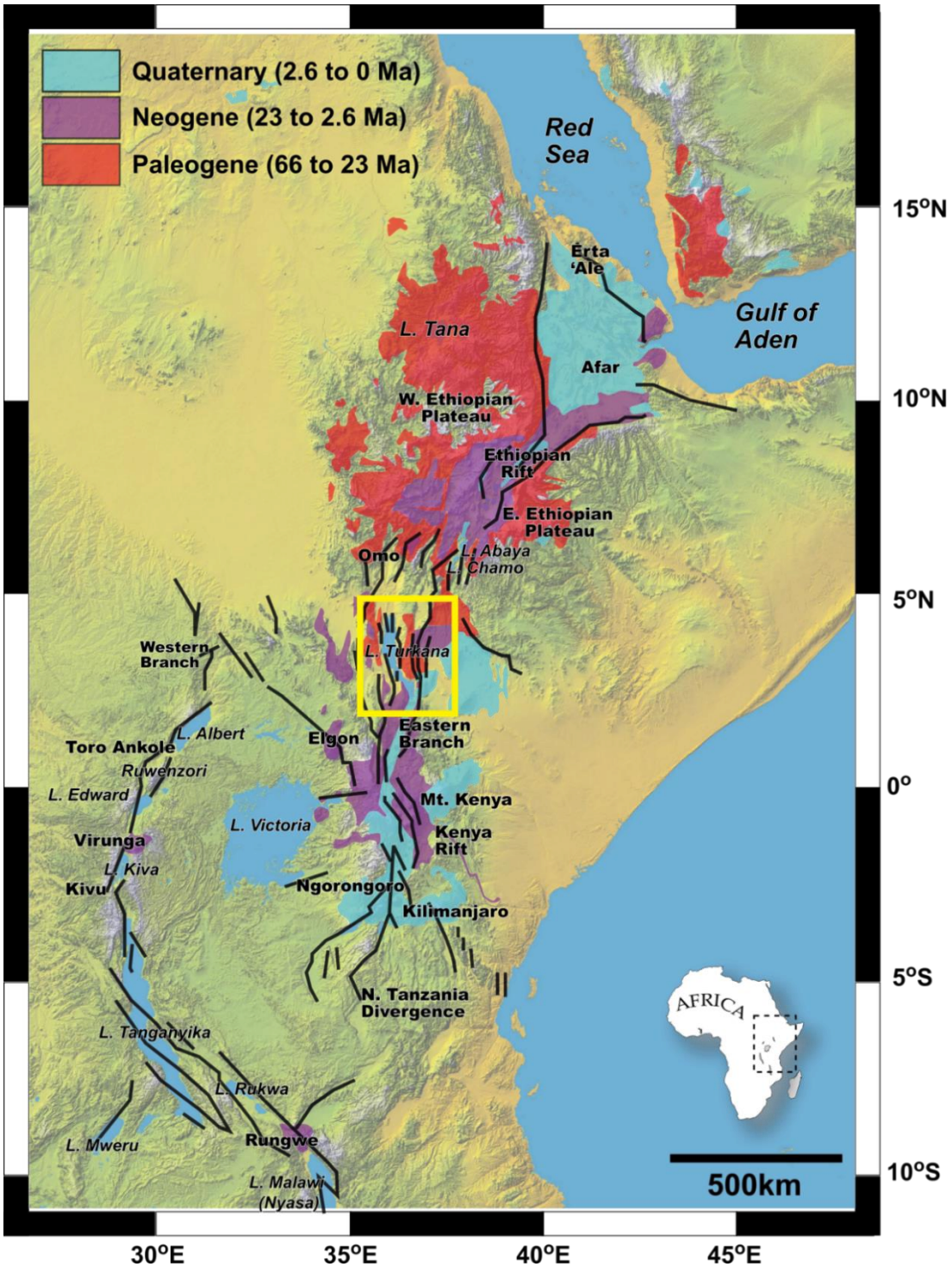

Figure 1. The East African Rift System (EARS) is comprised of two branches: Eastern and Western. The Easter branch begins in Afar and terminates in the Northern Tanzania Divergence, whereas the Western branch runs through Lake Albert to Lake Malawi (Chorowicz, 2005). This map also illustrates the magmatic events of the Cenozoic in East Africa. Yellow box refers to the area presented in Figure 2 (from Rooney, 2017).

within the EARS, but at a miniature scale. We propose that the melts that produced such widespread magmatism were generated by decompression melting during periods of lithospheric thinning. Trace element signatures overall show a continuity in sources between the Gombe Stratoid Series and Shield volcanoes, but as magmatism migrates towards Lake Turkana, melts of metasomatically enriched mantle begin to contribute to shield volcanism. These findings suggest the existence of regions of enriched lithosphere beneath Turkana, towards which magmatism and rifting migrated during the Pliocene. The implication of these findings is that the modern localized extension and magmatism within the Turkana Depression results from the focusing of extensional strain into a region where the plate contained enriched domains that facilitated melt formation within the plate. We suggest that these lithospheric melts effectively partitioned strain, localizing the formerly broad plate extensional processes.

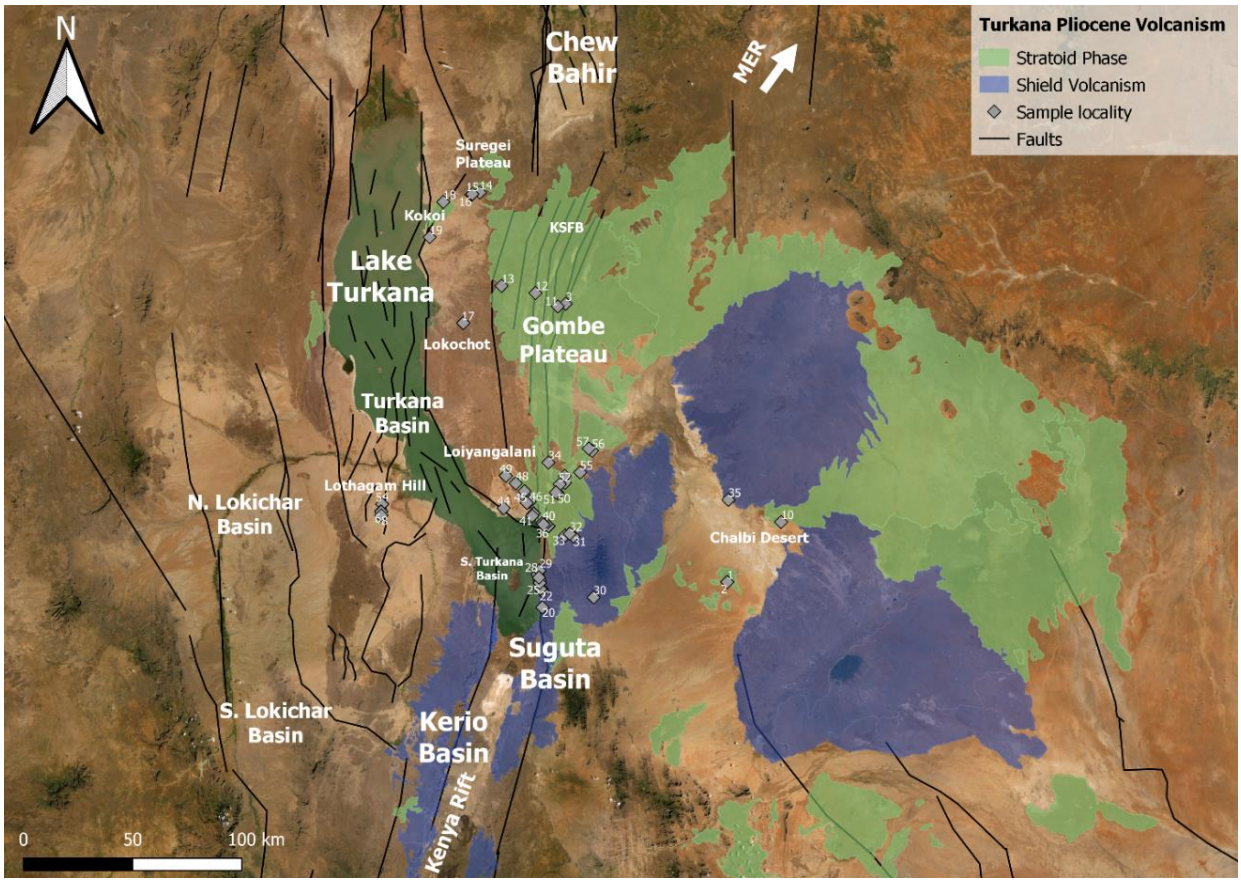

Figure 2. Pliocene magmatic activity in the Turkana Depression. Magmatism during this period is characterized by an initial episode of widespread volcanism (Stratoid Phase) that was subsequently followed by focused magmatism in the form of shield volcanoes (Shield volcanism). Samples from our study indicated by grey diamonds (see Table 1 for more details) KSFB = Kino Sogo Fault Belt; MER = Main Ethiopian Rift.

2. Background

2.1. Geologic History of the Turkana Depression

The Turkana Basin is located in the northern portion of the eastern branch of the EARS, incorporating approximately 131,000 km^2 of Northern Kenya and Southern Ethiopia (Furman et al., 2006; Feibel, 2011). Lake Turkana, located in Northern Kenya, occupies a significant portion of the basin, whereas the lower Omo Valley is incorporated within the Southern Ethiopian region of the basin (Haileab et al., 2004; McDougall and Brown, 2008). The basin has been an important locality for the investigation of fossil-bearing sedimentary strata, with stratigraphic and geochronological studies (e.g., Boschetto et al., 1992; McDougall and Feibel, 1999; McDougall and Brown, 2008, 2009; Gathogo et al., 2008; Brown and McDougall, 2011) providing a well-developed chronostratigraphic framework of the region.

The metamorphic basement of the Turkana Basin is mainly comprised of deformed schists and gneisses Pan-African in age (Brown and McDougall, 2011). Rearrangements of the crust in the interaction zone between the Kenyan and Main Ethiopian Rifts made the surface exposure of these rocks in the basin possible (Brown and McDougall, 2011). As noted by Feibel (2011), these rocks acted as the main sediment source of the clastic sequences that were deposited during the Neogene. In some areas of the basin, the basement rocks are overlain by sedimentary rocks that have been dated to the Cretaceous on the basis of their fossil content (Brown and McDougall, 2011).

As stated by Furman et al. (2006) and Feibel (2011), the Turkana Depression has an extensive history of rifting activity and basin development. These rifting episodes have resulted in its highly faulted morphology and thin continental crust (e.g., Ebinger and Ibrahim, 1994; Hendrie et al., 1994; Ebinger et al., 2000). Propagation of the Eastern (Kenya) rift and Main Ethiopian rift (MER) towards Turkana have also played a role in the structure of the Depression (e.g., Ebinger et al., 2000; Figure 2). The earliest evidence of rifting in the Turkana Depression is associated with the Central African Rift System (CARS), which developed during the Cretaceous (e.g., Bosworth, 1992). The CARS led to the development of the Anza Graben, which changed the lithospheric structure of Turkana, resulting in a crustal thickness of about 25 km (e.g., Rooney, 2020a). Several publications (e.g., Macgregor, 2015; Purcell, 2018) have compiled

existing data to reconstruct the history and evolution of the EARS. Within the Turkana region, an overall eastwards migration of rifting, strain and magmatism is observed (e.g., Morley et al., 1992; Ebinger et al., 2000; Vetel and LeGall, 2006; Macgregor, 2015). EARS rifting activity in the Turkana Depression began West of Lake Turkana with the development of North-South trending Paleogene rift structures that marked a change in the stress conditions (Macgregor, 2015; Purcell, 2018). In the Mid-Miocene, the Eastern rift propagated towards Lake Turkana (e.g., Morley et al., 1992; Hendrie et al., 1994). This eastwards propagation is also noted in the migration of rifting activity from South Lokichar basin towards North Lokichar, Kerio, and Lake Turkana, where a rifting center in the latter was developed during this time period (e.g., Macgregor, 2015; Purcell, 2018; Muirhead et al., 2022; see Figure 2 for basin locations). The North-South propagation of rifting from this center is suggested by Purcell (2018) to have occurred between 22-17 Ma, whereas Macgregor (2015) suggests a younger (Pliocene) age for rift propagation. As indicated by Purcell (2018), volcanic activity, polarity reversals due to the development of faults, and rift migration occurred within the Turkana Basin at ca. 13-10 Ma. Beginning in the early Pliocene, EARS-related subsidence took the form of alternating half-graben structures with a North-South trend (Feibel, 2011). The author also notes other significant pulses of tectonic activity during the Pleistocene period that led to the development of the Hamar Uplift, as well as the culmination of the modern basin configuration.

Volcanism in the Turkana Basin initiated in the Eocene and has extended to Recent times (e.g., Rooney, 2020a). Eocene volcanism was dominantly basaltic, though other volcanic products such as rhyolites and ignimbrites are also present (Brown and McDougall, 2011; Feibel, 2011; Rooney, 2017). These basaltic lavas have been identified in different localities within the basin (e.g., eastern and western shores of Lake Turkana, Nabwal Hills) and are often intercalated with sedimentary strata (Rooney, 2017; Feibel, 2011; Brown and McDougall, 2011). Volcanism in the Oligocene was widespread, with the most significant basaltic activity occurring on the western side of the basin, though isolated basalts are identified in other areas within the basin (Rooney, 2017). Silicic volcanism also occurred during this period (McDougall and Brown, 2009). Following the Oligocene flood basalt volcanism, magmatic activity in the basin manifested as a series of basaltic pulses (Rooney, 2020a). The first basaltic pulse – the Early Miocene Resurgence

Phase – began in Turkana and Southern Ethiopia ca. 24 Ma and lasted until ca. 17 Ma (Rooney, 2017; Rooney, 2020a). During this pulse of activity, the first instance of magmatism in the growing Kenya Rift – the Samburu Event – occurred, suggesting southwards migration of magmatism from Turkana towards this region (Rooney, 2020a). Silicic volcanism was prominent in some locations within the basin, and basaltic activity was restricted to the shores of the lake (Rooney, 2017). Sediment accumulation occurred in the basin during a hiatus in basaltic activity until ca. 16 Ma, when small-scale basaltic activity began (McDougall and Brown, 2009; Rooney, 2020a). This was followed by rhyolitic volcanism. The second pulse of basaltic magmatism (ca. 12 Ma – 9 Ma) is called the Mid Miocene Resurgence Phase and is characterized by widespread stratiform basalts (Rooney, 2020a). Basaltic activity from this pulse includes those identified on the western side of Lake Turkana (e.g., Lothidok and in the Nabwal Arangan Beds at Lothagam Hill) as well as south of Marsabit shield volcano (Rooney, 2020a and references therein). After this period of wide-scale basaltic activity, there was a hiatus in magmatism in the Turkana Basin (and Southern Ethiopia) that lasted ca. 5 Ma (Rooney, 2020a), which is broken by a final widespread basaltic pulse that is recorded during the Pliocene.

2.2. Stratoid Phase – Gombe Group and Pliocene shield volcanism:

After the 5 Ma hiatus, a new pulse of magmatic activity began in Turkana, Southern Ethiopia, and in the Kenya Rift (Rooney, 2020a). This period also marks the recommencement of tectonic activity in Turkana, with studies (e.g., Purcell, 2018; Macgregor, 2015) suggesting the reactivation is linked with deepening of the rift. The Stratoid Phase (ca. 4 Ma – 0.5 Ma) initiates with the Gombe Stratoid Series – a large volume basaltic event that is dated between 4.22 Ma – 3.97 Ma (Gathogo et al., 2008). Although the Gombe Group lavas are centered in Turkana, this group has been correlated with basalts from Southern Ethiopia: Mursi, Harr, and the Nkalabong Formation (Asfaw et al., 1991; Ebinger et al., 1993, 2000; Haileab et al., 2004). The areally extensive Gombe Series in Turkana was followed by spatially-limited basaltic activity in the form of shield volcanoes emplaced on top of the Gombe lava flows, with the main volcanic edifices located on the eastern shore of Lake Turkana: Longipi (3.5Ma-1.5Ma) (Furman et al., 2006), Kulal (3.01Ma-1.71Ma) (Ochieng and Wilkinson, 1988; Gathogo et al., 2008), and Asie (2.7Ma-2.07Ma ± 0.13)

(Key et al., 1987). In addition to these edifices, the Bulal basalts (3.2 Ma) (Ebinger et al., 2000), Marsabit shield (1.70Ma-0.76Ma) (Key et al., 1987), and the Huri Hills are also part of this shield phase activity (Rooney, 2020a).

Lavas from the Gombe Group are described by Haileab et al. (2004) as dominantly aphyric basalts intercalated with thin layers of sediments. These lavas are mainly exposed on the Suregei and Gombe Plateaus in the Turkana Depression (Figure 3) as well as in the Omo Valley (Mursi basalts) and small plateaus (Harr) in Ethiopia (Haileab et al., 2004). Other exposures east of Lake Turkana include those found in the Kokoi Highland intruding the Lonyumun Member of the Koobi Fora Formation (Haileab et al., 2004). To the west of Lake Turkana, basalts such as those at Lothagam Hill have also been included as part of the Gombe Group by Haileab et al. (2004). These basalts, known as the Lothagam Basalt, have been previously given a suggested maximum age of 4.20 Ma by McDougall and Feibel (1999), but a recent study by Rowan (2021) has redated the Lothagam Basalt at 3.84 ± 0.04 Ma.

The volcanic edifices that followed the Gombe Group (Longipi, Kulal, Asie) are located along the eastern side of Lake Turkana and follow an en echelon arrangement (Figure 3) (Rooney, 2020a). Younger monogenetic cones, maars and flows are located on top of the shields, whereas monogenetic fields of similar age occur between them (Key and Watkins, 1988; Rooney, 2020a). These younger features extend to Ethiopia (Rooney, 2020a). Compositionally, the shields are made up of olivine-plagioclase phyric or clinopyroxene-olivine phyric basaltic flows (Rooney, 2020a). The Namarunu shield volcano in the Kenya Rift is associated with the Lorikipi Basalts (4.0 Ma – 2.33 Ma), and it is thought that these basalts are also linked to this shield building phase (Dunkley et al., 1993; Rooney, 2020a). In the Loiyangalani region, there are three basaltic units found within the Koobi Fora Formation: the ca. 3.3 Ma – 3.2 Ma Kankam basalt, the Lenderit basalt (2.18 Ma – 2.02 Ma), and the 1.79 Ma Balo basalt (Gathogo et al., 2008). As presented by the authors, these basalts are correlated with the Pliocene shield-building phase.

3. Methodology

3.1. Samples and sample preparation

This project was conducted using two sample suites that include rocks from the Gombe Stratoid Series lavas and the Pliocene shield volcanoes (Table 1). The suite collected by Frank Brown consists of 25 samples from the Gombe Group lavas and 21 pertaining to the Pliocene Shields. The second sample suite used in this project was collected by Neil Opdyke (Opdyke et al., 2010). This suite contains 20 core samples from the Loiyangalani region that correspond to the Pliocene Shield-building phase. Geochemical data was collected for 15 of these samples, but all 20 samples were used to describe the petrography of the group they correspond to. High resolution thin section scans of samples from both suites were produced using PiAutoStage (Steiner and Rooney, 2021) to facilitate the petrographic analysis portion of this study.

To obtain major and trace element data, samples from the Frank Brown suite were originally cut into billets and polished to remove saw marks. To eliminate any possible contamination, the samples were then cleaned in an ultrasonic bath using de-ionized water. These samples were powdered using a BICO flat plate pulverizer with ceramic plates. In contrast, core samples from the Opdyke suite were initially polished to remove contaminants in the surface of the cores. The samples were then crushed using the Sepor Model 150 Mini Jaw Crusher, and the sample chips were hand powdered using an agate mortar and pestle. For each sample, a homogeneous glass disc was fused using the rock powder and lithium tetraborate flux, following the procedure of Rooney et al. (2012a).

3.2. Analytical Work

Geochemical analyses were conducted at Michigan State University using X-ray fluorescence (XRF) and laser ablation inductively coupled plasma mass spectrometry (LA-ICP-MS) for major and trace elements, respectively. The fused discs were analyzed for major elements using a Bruker S4 Pioneer XRF. The instrument was calibrated using rock standards that have also been fused into glass discs. The same sample fused discs were analyzed for trace elements using a Photon Machines Analyte G2 Excimer and Thermo iCAPQ Quadrupole ICP-MS and following the methodology of Rooney et al. (2012a). These data were collected over a total of five sessions in which the standards were run multiple times as unknowns.

Samples were ablated by a 193 nm laser (spot size: 110 microns) for a total of 120 seconds. Each sample was run three times and the individual runs were averaged to obtain trace element concentrations. In addition, each session included a sample replicate as part of the analysis, with a total of 5 replicates of different samples.

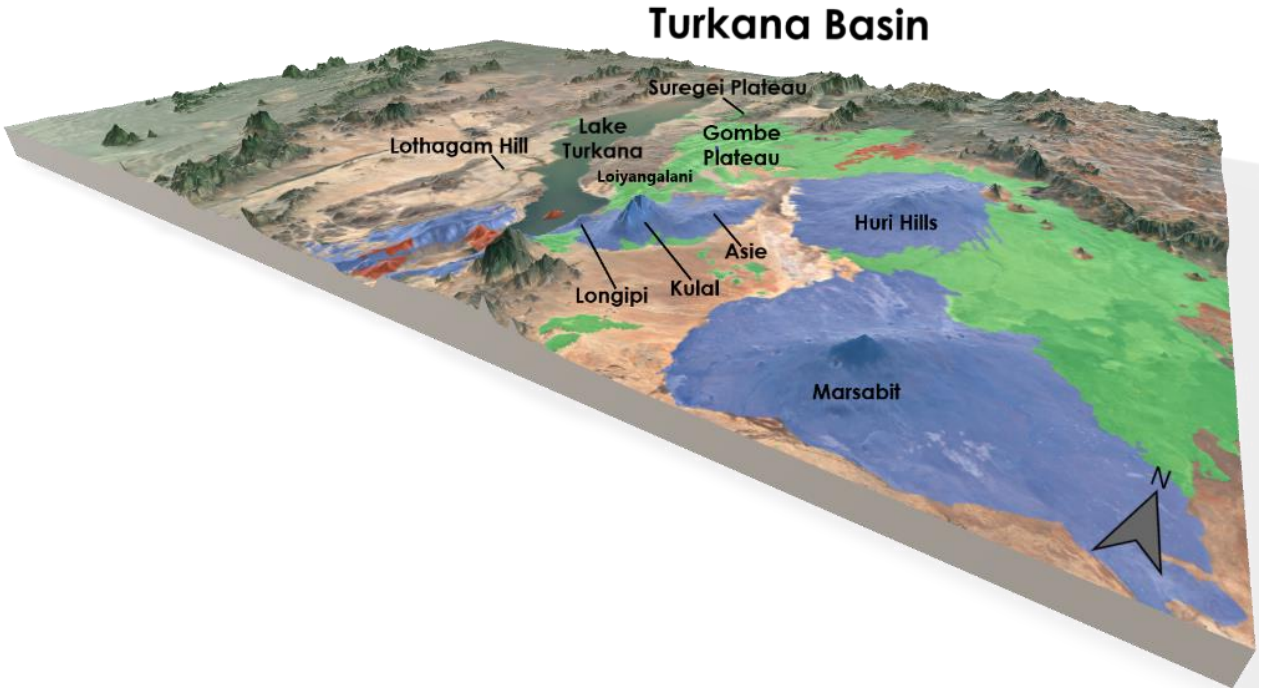

Figure 3. Topographic 3D rendering of the Turkana Basin, looking West towards Lake Turkana, showing the distribution of the Stratoid Phase, a new pulse of magmatism after a 5 Ma hiatus. Magmatism during this period is characterized by an initial episode of widespread volcanism (Gombe Stratoid Series - green) that commenced ca. 4 Ma (Rooney, 2020a). These lavas are mainly exposed in the Gombe and Suregei Plateaus, as well as other localities such as Lothagam Hill (Haileab et al., 2004). This volcanism was subsequently followed by small scale shield volcanism (blue). The Longipi, Kulal, and Asie shield volcanoes are located on the Eastern shore of Lake Turkana and follow an en-echelon formation (Rooney, 2020a). The Huri Hills and Marsabit are also part of this magmatic event (Rooney, 2020a). The Gombe and shield phases represent the last stages of lithospheric thinning in the basin prior to a new phase of magmatism that represents a period focused intrusion (Axial Phase – red; not part of this study).

Table 1. List of samples and localities used in this study.

Gombe Stratoid Phase				
IGSN	**Lat**	**Lon**	**Locality**	**No. in map (Fig. 2)**
Hoi Basalt				
TOR0000OU	2.6255	37.4715	Chalbi Desert	1
TOR0000OV	2.625	37.4711	Chalbi Desert	2
TOR0000OT	2.6255	37.4715	Chalbi Desert	1
TOR0000OH	3.7689	36.806	Gombe Plateau	3
Gombe A				
TOR0000NW (Lothagam Basalt)	2.946	36.051	Lothagam Hill	4
TOR0000NI (Lothagam Basalt)	2.914	36.046	Lothagam Hill	7
TOR0000ND (Lothagam Basalt)	2.8993	36.0469	Lothagam Hill	8
TOR0000NH (Lothagam Basalt)	2.914	36.046	Lothagam Hill	7
TOR0000NV (Lothagam Basalt)	2.9451	36.0503	Lothagam Hill	5
TOR0000NC (Lothagam Basalt)	2.8993	36.0469	Lothagam Hill	8
TOR0000NX (Lothagam Basalt)	2.9155	36.0458	Lothagam Hill	6
TOR0000O0	2.982	36.633	Loiyangalani	9
TOR0000NS	2.872	37.693	Chalbi Desert	10
TOR0000OE	3.8132	36.6817	Gombe Plateau	12
TOR0000NA	4.2269	36.4522	Suregei Plateau	14
TOR0000OG	3.7584	36.7735	Gombe Plateau	11
TOR0000OD	3.8427	36.542	Gombe Plateau	13
TOR0000O3	3.6898	36.3842	Lokochot - E Lake Turkana	17
Gombe B				
TOR0000OX	4.2174	36.4186	Suregei Plateau	16
TOR0000O6	4.1879	36.302	Kokoi Highland	18
TOR0000O4	3.6898	36.3842	Lokochot - E Lake Turkana	17
TOR0000OZ	4.2203	36.4219	Suregei Plateau	15
TOR0000OC	4.0433	36.2461	Kokoi Highland	19
TOR0000NJ (Lothagam Basalt)	2.914	36.046	Lothagam Hill	7
TOR0000NB (Lothagam Basalt)	2.8993	36.0469	Lothagam Hill	8
Pliocene Shield volcanoes and correlated basaltic lava flows				
IGSN	**Lat**	**Lon**	**Locality**	**No. in map (Fig. 2)**
Longipi Shield				
TOR0000O1	2.521	36.71	Loiyangalani	20
TOR0001DH	2.6557	36.691	Loiyangalani	28
TOR0001DP	2.5962	36.7065	Loiyangalani	22
TOR0001DM	2.6722	36.6977	Loiyangalani	29
TOR0001DK	2.5883	36.7098	Loiyangalani	21
TOR0001DI	2.5967	36.702	Loiyangalani	24
TOR0001DJ*	2.5967	36.702	Loiyangalani	23
TOR0001DN*	2.6327	36.6988	Loiyangalani	26
TOR0001DO*	2.6215	36.6993	Loiyangalani	25
TOR0001DQ*	2.6437	36.696	Loiyangalani	27
Kulal Shield				
TOR0000N9	2.562	36.921	Loiyangalani	30
TOR0001DL	2.8168	36.804	Loiyangalani	33
TOR0001D8	2.8122	36.8382	Loiyangalani	31
TOR0001D9	2.8237	36.8227	Loiyangalani	32

Table 1 (cont'd)

Asie Shield					
	TOR0000NR	3.1166	36.7348	Loiyangalani	34
Huri Hills					
	TOR0000OW	2.9633	37.4759	Huri Hills - Chalbi Desert	35
Kankam Basalt					
	TOR0000OR	2.8545	36.7358	Loiyangalani	36
	TOR0000OQ	2.8551	36.7351	Loiyangalani	37
	TOR0000OP	2.8551	36.7351	Loiyangalani	37
	TOR0000OL	3.0758	36.8657	Loiyangalani	55
	TOR0000OK	3.0334	36.803	Loiyangalani	53
	TOR0000OJ	3.1646	36.9145	Loiyangalani	56
	TOR0000NE	2.99	36.773	Loiyangalani	50
	TOR0000OO	2.8636	36.7255	Loiyangalani	38
	TOR0000OA	2.9068	36.6745	Loiyangalani	42
	TOR0001DC	3.0613	36.8025	Loiyangalani	54
	TOR0001DD	2.9062	36.6738	Loiyangalani	43
	TOR0001DB*	3.0272	36.7818	Loiyangalani	52
Lenderit Basalt					
	TOR0000OI	3.1738	36.9015	Loiyangalani	57
	TOR0000NZ	2.9986	36.6364	Loiyangalani	47
	TOR0000O7	2.8682	36.7107	Loiyangalani	40
	TOR0000NY	2.9547	36.6577	Loiyangalani	46
	TOR0000O9	2.9504	36.6461	Loiyangalani	45
	TOR0001DG	2.8618	36.7145	Loiyangalani	39
	TOR0001DF	2.9288	36.5508	Loiyangalani	44
	TOR0001DE	2.8973	36.6683	Loiyangalani	41
	TOR0001D7	3.031	36.6003	Loiyangalani	48
	TOR0001DA	2.9937	36.766	Loiyangalani	51
Balo Basalt					
	TOR0000ON	3.0618	36.5597	Loiyangalani	49

*Samples only used for petrographic analysis; no geochemical data available

4. Results

4.1. Gombe Group lavas

Lavas from the Gombe Stratoid Series are divided into three groups: Gombe A, Gombe B, and Hoi (see Table 1). These groups were identified on the basis of petrography as well as geochemistry. Below is a detailed description of the petrography and geochemistry of each group:

4.1.1. Petrography

Gombe A and Gombe B groups are made up of plagioclase, clinopyroxene, and oxides; however, their textures vary significantly, as described below. Basalts from Hoi are also made up of plagioclase, clinopyroxene, and oxides, but unlike Gombe A and B, they also contain olivine.

Gombe A group: Many of the samples in Gombe A group are part of the Lothagam Basalts (see Table 1). These samples – except for TOR0000NX – are characterized by plagioclase phenocrysts and 'bow-tie' plagioclase intergrowth with clinopyroxene (Figure 4a-b). This 'bow-tie' texture is indicative of cotectic crystallization between these two minerals (e.g., Bryan, 1979; Thy, 1983). Plagioclase phenocrysts are tabular and mostly subhedral, with simple or polysynthetic twinning and/or zoning present. Microphenocrysts of oxides are also present. The groundmass of these samples is composed of plagioclase, clinopyroxene and oxides. The rest of the samples from the Gombe A group, including TOR0000NX, are characterized by plagioclase and minor clinopyroxene phenocrysts, as well as glomerocrysts made up of the same minerals; although rare, some glomerocrysts also include oxides. Within these glomerocrysts, plagioclase also occurs as 'bow-tie' intergrown with clinopyroxene. Plagioclase phenocrysts are mostly subhedral and tabular. These crystals show simple or polysynthetic twinning and some also exhibit zoning. Clinopyroxene is mostly subhedral with zoning present in some crystals. The groundmass of these samples varies from glassy to intergranular, the latter being composed of plagioclase laths, clinopyroxene, and oxides. The modal composition of the Gombe A group is ~55% plagioclase, ~35% clinopyroxene and ~10% oxides.

Gombe B group: Samples from this group are glomerophyric (Figure 4c-d), with the exception of one sample that is part of the Lothagam basalts (TOR0000NB). This sample is characterized by the same 'bow-

tie' plagioclase growth in clinopyroxene and plagioclase phenocrysts that is dominant in the Gombe A group. The rest of the samples from the Gombe B group are characterized by a glassy or fine grained groundmass. The glomerocrysts are mostly made up of clinopyroxene and plagioclase, and oxides are commonly found within the glomerocrysts. The 'bow-tie' plagioclase growth is also identified in glomerocrysts. Monomineralic (i.e., clinopyroxene or plagioclase) glomerocrysts are also seen, but these are less common than the former. Phenocrysts of clinopyroxene as well as plagioclase are common. Clinopyroxene ranges from anhedral to subhedral and some crystals exhibit zoning. Plagioclase is tabular with simple or polysynthetic twinning. Some plagioclase phenocrysts are partially dissolved, indicating these crystals are not in equilibrium. The groundmass of Gombe B is dominantly glassy with thin plagioclase laths/needles. The modal composition of the Gombe B group is ~45% clinopyroxene, ~35% plagioclase, ~10% oxides and ≤5% glass.

Hoi: These basalts are characterized by plagioclase phenocrysts and cotectic crystallization of plagioclase and clinopyroxene. Additionally, partially to completely altered subhedral olivine phenocrysts were identified in one of the Hoi samples (TOR0000OH; see Figure 4e-f). Although not abundant, this sample also contains glomerocrysts made up of plagioclase with clinopyroxene or olivine. Plagioclase phenocrysts found in the Hoi basalts are tabular and elongated ranging from subhedral to euhedral. These phenocrysts are also characterized by either simple or polysynthetic twinning, with zoning present in some of them. Clinopyroxene phenocrysts range from anhedral to subhedral, and some of these also exhibit zoning. Oxide microphenocrysts are also present throughout the Hoi samples, except TOR0000OH, in which they are only found as part of the groundmass. The groundmass of Hoi is intergranular and made up of plagioclase laths/needles, clinopyroxene, oxides, and minor amounts of glass. Hoi basalts have a modal composition of ~55% plagioclase, ~30% clinopyroxene, ~10% oxides, ~5% olivine and ≤1% glass.

4.1.2. Geochemistry

Major and trace element data of the Gombe A and B groups exhibit moderately evolved compositions, with 3.5-5.0 wt.% MgO. These lavas are also characterized by high TiO_2 (~3.2-3.8 wt. %), which is uncommon for other lavas in the region (see Rooney 2020a; Figure 8). Despite their overall "clustering",

these two groups can be distinguished on the basis of their MgO content, as described below. Basalts from the Hoi group, in contrast, have slightly more primitive compositions than Gombe A and B (see below).

Gombe A group: Lavas from this group all have MgO > 4 wt. % and are characterized by an overall increase in major elements as MgO decreases, with the exception of CaO, Al_2O_3, and FeO (all in wt. %). Trace element signatures (ppm) show an increase in REE and other incompatible trace element concentrations – except Sr – with decreasing MgO (wt. %), but a decrease in compatible trace element concentrations.

Gombe B group: This group is made up of the most evolved lavas within the Gombe Stratoid Series, with MgO ≤4 wt. %. These lavas exhibit higher CaO and Al_2O_3 and lower Na_2O (all wt. %) than Gombe A group. The behavior of CaO and Na_2O in this group is worth noting: CaO increases with increasing MgO in a curved manner, whereas Na_2O decreases in an almost vertical trend (see Figures 8 and 11). Although Gombe B lavas also show an increase in REE and other incompatible trace element concentrations, except Sr, their values are more consistent (i.e., they are clustered). Like Gombe A lavas, the compatible trace elements also show a decreasing trend, but the clustered behavior of Gombe B is not seen in Co (ppm) in which the decrease is more scattered and nearly vertical. Another distinct signature from Gombe B is seen in V (ppm), where a decrease at higher MgO is followed by a gradual increase exhibited by the more evolved samples of this group. It is also noteworthy that for some trace elements, such as Sc, Rb and Ba, there are no significant differences among Gombe A and Gombe B (i.e., both fall within the same ppm range).

Hoi: Major and trace element data from the Hoi basalts show that they are slightly more primitive than Gombe A and B lavas, with 5.7-5.9 wt. % MgO (Figure 8). Hoi is also relatively high in TiO_2 (~3.0-3.5 wt. %) in comparison to other regional basalts, however, they are lower in TiO_2 than the exceptionally high concentrations observed in Gombe A and B. With respect to CaO (wt. %), Hoi is more enriched than both Gombe Groups, but all three groups exhibit similar concentrations of Al_2O_3 (wt. %). Hoi exhibits an enrichment in compatible elements such as Ni and Co, but it is depleted in incompatible trace elements relative to Gombe lavas.

Primitive mantle normalized diagrams (Sun and McDonough, 1989; Figure 9) show peaks in Ba, Nb-

Ta and negative anomalies in Th-U, K, Sr in the three Gombe Groups. However, a negative Ti anomaly is found in Gombe A and Gombe B, the latter having a more pronounced anomaly than the former group. This anomaly is not identified in Hoi, which appears to have a "peak" in Ti relative to Gombe A and B. The pattern for the three Gombe Groups broadly represents a magma Type III pattern, which is characterized by its peaks in Ba and Nb-Ta, and a trough in Th-U (Rooney, 2020d). Chondrite normalized diagrams (Figure 10) for the three groups broadly follow the same trend, where they are relatively more enriched in LREE than HREE. A small negative Eu anomaly is present in Gombe A and B, but not in the Hoi basalt, and is likely controlled by plagioclase fractionation. Although the three groups overall follow the same trend in chondrite normalized diagrams, the Hoi basalt patterns are less enriched than those of Gombe A and B groups.

4.1.3. Characterization of textures in the Gombe Groups and their effect on geochemistry

As noted above, Gombe A dominantly exhibits cotectic texture while Gombe B is dominated by a glomerophyric texture (6 out of 7 samples). Despite this, glomerocrysts are still present in some samples that are part of the Gombe A group (6 out of 14 samples). To determine the abundance of glomerocrysts in Gombe A and Gombe B, a similar approach to that described by Humphreys et al. (2013) was used. Glomerocrysts were identified using ImageJ software (Schneider et al., 2012), where each glomerocryst was outlined by drawing a polygon around it to obtain its area. The area of each glomerocryst was given in pixels and was then converted to m^2 based on the amount of pixels per meter of the high resolution thin section scans (507,000 pixels/meter). In addition to quantifying the amount of glomerocrysts per thin section, this method allowed us to calculate the total area occupied by glomerocrysts per thin section (see Table 2 for details). To do this, the individual areas of each glomerocryst per sample were summed to obtain the total area of glomerocrysts in a given thin section. This value was then divided by the area of the thin section scan (0.0015 m^2) to obtain the area (%) occupied by the glomerocrysts in the thin section.

A total of 137 glomerocrysts were identified in the Gombe A group, whereas a total of 212 glomerocrysts were identified in the Gombe B group. Based on the area calculations, the total percentage of glomerocrysts in the Gombe A group is about 0.18%. In contrast, the total percentage of glomerocrysts

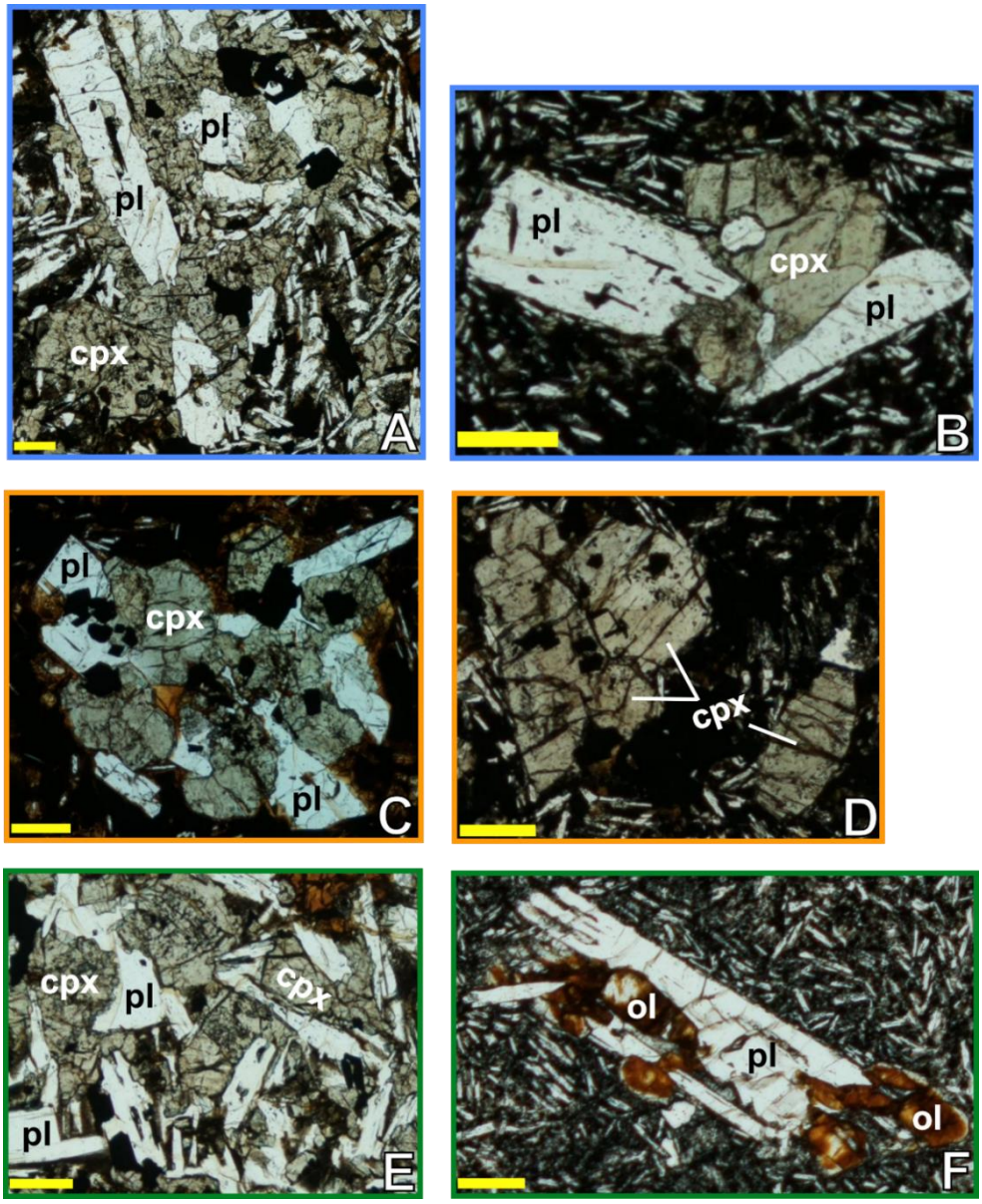

Figure 4. Petrography of the Gombe Stratoid Series groups. (A, B) PPL images of textures identified in the Gombe A group. (A) Cotectic texture between plagioclase and clinopyroxene, where plagioclase is seen as a "bow-tie". (B) Glomerocryst of the Gombe A Group made up of plagioclase and clinopyroxene. (C, D) PPL images of glomerophyric texture of Gombe B group. (C) Polymineralic glomerocryst made up of plagioclase, clinopyroxene, and oxides set in a glassy groundmass. (D) Clinopyroxene glomerocryst and phenocryst. Note also the presence of small oxides in the glomerocrysts as well as zoning in clinopyroxene crystals. (E,F) PPL images of Hoi. (E) Cotectic crystallization of plagioclase and clinopyroxene (F) Plagioclase and olivine glomerocryst set in a microcrystalline groundmass. Note the partially to completely altered olivine phenocrysts. Scale = 200 microns in all images. cpx = clinopyroxene; pl = plagioclase; ol = olivine.

in the Gombe B group is about 0.64% (Table 2). These calculations show that despite glomerocrysts being present in both groups, they are significantly more abundant in Gombe B. It is important to note, however,

that these values are minimum estimates rather than a full representation of each group, given that the thin sections available for this study are representative of a small portion of the sample/lava flow.

The differences in abundance and compositions of glomerocrysts between the two groups ultimately have an effect on the behavior of major and trace elements. Compositionally, glomerocrysts in both groups are mostly made up of plagioclase and clinopyroxene, however, oxides are also a common phase in glomerocrysts of the Gombe B group and far less common in those from Gombe A. Monomineralic glomerocrysts are not nearly as common than polymineralic ones, but these were only identified in the Gombe B group. Accumulation of plagioclase and pyroxene will have an effect on the concentrations of Al_2O_3 and CaO. Geochemistry of the Gombe B lavas shows that this group is more enriched in these major elements than Gombe A. Plagioclase and clinopyroxene-rich glomerocrysts have played a role in making this group more enriched in these elements as MgO decreases. This would also explain the decreasing behavior of Na_2O in Gombe B relative to Gombe A, as the accumulation of these phases will result in a decrease in Na_2O due to the enrichment in other major elements. In contrast, oxides have an effect in the behavior of transition metals, such as V and Mn, which are favored in these minerals. The accumulation of oxides could thus explain the behavior of V in the Gombe B group, where this trace element decreases and then begins to gradually increase as more evolved compositions are reached.

4.2. Pliocene Shield volcanoes and correlated basaltic lava flows

Shield volcanoes that followed the widespread Gombe Stratoid Series include: Longipi, Kulal, Asie, and Huri Hills. As noted in section 2.2 (see also Table 1), there are three basaltic units within the Loiyangalani region that are also part of the shield volcanism phase: Kankam, Lenderit, and Balo. A detailed description of the petrography and geochemistry of each of these edifices and correlated basaltic units is as follows:

4.2.1. Petrography

Longipi Shield: Longipi Shield samples (Figure 5a-c) vary from fine-grained to porphyritic-coarse grained, and some are vesicular. Compositionally, these are mainly olivine-phyric, but clinopyroxene and plagioclase are major and minor phases in porphyritic samples respectively. Olivine crystals vary from

anhedral to euhedral, ranging in size from 0.2mm up to about 3mm in porphyritic samples. Iddingsite alteration along the rims of smaller olivine phenocrysts is common, but a few of the larger olivine phenocrysts exhibit alteration by a different mineral thought to be bowlingite. Plagioclase phenocrysts (up to ~1.5mm width in porphyritic samples) are tabular with polysynthetic twinning, and zoning is sometimes present. Clinopyroxene phenocrysts, most likely augite, are mainly subhedral and often show zoning. These range in size from 0.3mm to about 2.5mm. Glomerocrysts of olivine and/or clinopyroxene are common in porphyritic samples. The majority of the samples have microcrystalline groundmass, but intergranular texture has also been identified. Said groundmass is made up of plagioclase laths, olivine, clinopyroxene, oxides, and glass. Overall, Longipi Shield samples have a modal composition of ~55% olivine, ~25% plagioclase, ~15% clinopyroxene and ~5% oxides and glass.

Table 2. Number and area of glomerocrysts in Gombe A and Gombe B groups.

Gombe A group (6 out of 14 samples contain glomerocrysts)			
Sample	**Number of glomerocrysts**	**Total Area (m²)**	**Area occupied in thin section (%)***
TOR0000O0	10	1.78E-06	0.12
TOR0000O3	60	1.33E-05	0.88
TOR0000OD	14	3.83E-06	0.26
TOR0000NS	17	5.88E-06	0.39
TOR0000NX	18	4.102E-06	0.27
TOR0000OG	18	9.85E-06	0.66
	% glomerocrysts in Gombe A group:		**0.18**
Gombe B group (6 out of 7 samples contain glomerocrysts)			
Sample	**Number of glomerocrysts**	**Total Area (m²)**	**Area occupied in thin section (%)***
TOR0000NJ	38	1.65E-05	1.10
TOR0000O4	23	6.32E-06	0.42
TOR0000O6	27	1.13E-05	0.75
TOR0000OC	29	1.31E-05	0.87
TOR0000OX	33	7.76E-06	0.52
TOR0000OZ	62	1.27E-05	0.85
	% glomerocrysts in Gombe B group:		**0.64**

*Area of thin section = 0.0015 m²

Kulal Shield: Samples from the Kulal shield (Figure 5d-e) are olivine and plagioclase-phyric, with minor clinopyroxene present in sample TOR0001D8. Olivine phenocrysts are subhedral and less commonly

euhedral, varying in size from about 0.2mm to 1mm. The smaller olivine tends to exhibit more iddingsite alteration – some partially to completely altered – than the larger phenocrysts, in which alteration only occurs along the rims. Plagioclase occurs as laths and small (about 0.2mm width) tabular crystals that often exhibit twinning and sometimes show flow alignment. The groundmass of the samples varies from microcrystalline to intergranular, with a composition of plagioclase, oxides, clinopyroxene, and glass. The modal composition of Kulal is ~45% plagioclase, ~40% olivine, ~10% clinopyroxene and ~5% oxides and glass.

Asie Shield: Only one Asie shield sample was available for this study. This sample is a sparsely vesicular, olivine-phyric basalt with intergranular groundmass (Figure 5f). Olivine phenocrysts vary from subhedral to euhedral, with sizes ranging from 0.2mm to about 1.5mm. These often occur as aggregates. Some phenocrysts exhibit incipient iddingsite alteration along rims, and a few are partially to completely altered by the same mineral. The intergranular groundmass is made up of thin plagioclase laths, clinopyroxene – likely to be augite, and opaque oxides. The modal composition of this sample is 55% olivine, 35% plagioclase, ~8% clinopyroxene and ≤2% oxides.

Huri Hills: Similar to Asie, only one sample the sample from Huri Hills was available for our study. This sample is an olivine-phyric basalt with intergranular groundmass (Figure 5g). Olivine phenocrysts (up to ~1mm width) are mainly subhedral and occur as glomerocrysts and single crystals. Larger phenocrysts exhibit incipient iddingsite alteration along rims and fractures, but some of the smaller olivine are partially to completely altered. Microphenocrysts of clinopyroxene are sparse, as this phase is mainly found in the groundmass. Other phases that make up the intergranular groundmass are plagioclase, which occurs as laths, and oxides. Compositionally, this sample is ~45% olivine, ~45% plagioclase, ~8% clinopyroxene and ≤2% oxides.

Kankam Basalt: Kankam samples can be divided into three textural groups: microcrystalline, ophitic, and intergranular (Figure 6). Compositionally, Kankam is overall olivine-phyric. Olivine ranges in size from about 0.2mm-1.0mm and is mostly subhedral. This mineral occurs as single microphenocrysts in microcrystalline samples and as cumulates in intergranular and ophitic samples. In microcrystalline

samples, olivine is partially to completely altered by iddingsite, whereas in the other groups, alteration only occurs along rims and/or fractures. Plagioclase is another major phase in the three groups, occurring mainly as laths, but also with tabular habit, exhibiting polysynthetic twinning and in some cases zoning. Clinopyroxene is only a major phase in ophitic samples, where large (about 1.5mm-2mm length), tabular, and most likely augite crystals enclose thin plagioclase laths. This mineral is a minor phase in the other textural groups, mainly found in the groundmass, and occurring as phenocrysts and glomerocrysts with plagioclase in only one microcrystalline sample (TOR0001DB). Although uncommon, glomerocrysts of olivine and plagioclase have also been identified. The groundmass of Kankam is made up of plagioclase, clinopyroxene, and opaque oxides. Overall, Kankam basalts are ~55% olivine, ~30% plagioclase, ~10% clinopyroxene and ≤5% oxides.

Lenderit Basalts: Lenderit are plagioclase-phyric vesicular basalts (Figure 7a-c). Plagioclase crystals (>55%) range from subhedral to euhedral, often with a tabular habit. They also exhibit simple or polysynthetic twinning. Although not as dominant as plagioclase, clinopyroxene and olivine – mostly subhedral microphenocrysts – are present in some samples, where clinopyroxene often exhibits zoning and olivine is partially to completely altered by iddingsite. The groundmass of Lenderit varies from microcrystalline to intergranular. It is made up mostly of plagioclase, as well as oxides, clinopyroxene, and glass. The modal composition of the Lenderit basalts is >55% plagioclase, ~25% clinopyroxene, ~15% olivine and ≤5% oxides.

Balo Basalt: Our suite only contains one sample for Balo. The Balo basalt is relatively porphyritic and vesicular, with calcite crystallizing along the rims of the vesicles. This basalt is plagioclase and olivine-phyric (Figure 7d-e). The plagioclase crystals are subhedral to euhedral and tabular in shape, exhibiting simple or polysynthetic twinning. The olivine crystals are mostly subhedral and partially to completely altered by iddingsite. Some glomerocrysts of olivine crystals and olivine and plagioclase are present. The groundmass of the sample is microcrystalline and made up of plagioclase, clinopyroxene, minor olivine, and oxides. The modal composition of the Balo basalt is ~55% plagioclase, ~35% olivine, ~5% clinopyroxene and ~5% oxides.

4.2.2. Geochemistry

Longipi Shield: The Longipi shield exhibits primitive compositions with ~10 wt. % MgO for all samples except for one (~6 wt. % MgO; Figure 8). Apart from the lower MgO (wt. %) sample, which plots along samples from the Kankam basalts (see below; Figure 8), Longipi samples appear to be relatively consistent (i.e., clustering) in their major and trace element concentrations, with the exception of CaO (wt. %), Sr (ppm), Rb (ppm), and U (ppm), where concentrations are more scattered. Primitive mantle normalized plots (Figure 9) show Ba and Nb-Ta peaks, as well as negative peak in U, K and Ti. However, there are certain samples that exhibit some deviations from the overall signatures previously described: two samples lack the Ba and negative U peaks, three show a peak in Sr, and one sample displays a peak in Nd. Despite these deviations, most samples from Longipi broadly follow a Type III magma pattern, but the lack of a Ba peak and negative U peak is more representative of a magma Type IV pattern (see Rooney, 2020d). A relative enrichment in LREE than HREE is seen in chondrite normalized diagrams for Longipi (Figure 10).

Kulal Shield: Kulal shield shows more compositional variability than Longipi. These samples range between ~5-12 MgO (wt. %) and show an overall decrease in compatible trace elements and an increase in most incompatible trace elements with decreasing MgO (wt. %) except Sr (ppm) (Figure 8). Other incompatible elements (e.g., Rb, Pb, Ba) show somewhat consistent concentrations regardless of MgO (wt. %). Trace element patterns in primitive mantle normalized plots (Figure 9) for Kulal are characterized by Ba and Nb-Ta peaks, Th-U trough, as well as a negative K peak. A Ti peak is exhibited by one of the Kulal samples, but this is not seen in the rest of the lavas from this group. The overall signatures exhibited by Kulal lavas are in agreement with a magma Type III pattern (Rooney 2020d). Chondrite normalized diagrams show an overall enrichment in LREE relative to HREE. However, there are two samples that appear to be more depleted in HREE than the rest (Figure 10).

Asie Shield: The sample from Asie has a primitive composition, with about 12 wt. % MgO (Figure 8). We are unable to identify any major and trace element trends with only one sample, but we can look at the trace element patterns in a primitive mantle normalized diagram to obtain information about their possible magma type. The primitive mantle normalized pattern for Asie is characterized by a Th-U trough and Nb-

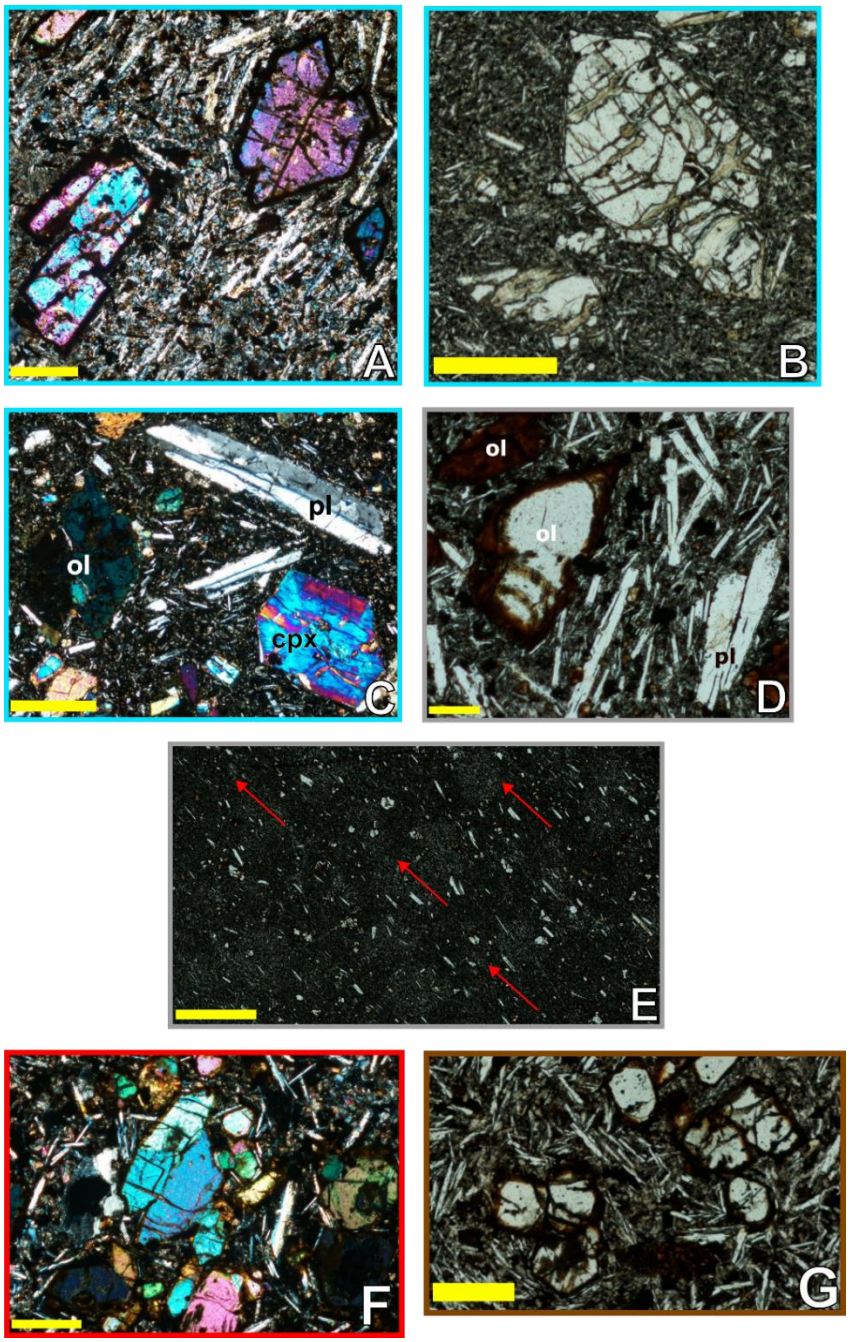

Figure 5. Petrography of Longipi (A-C), Kulal (D-E), Asie Shield (F) and Huri Hills (G). (A) XPL image of euhedral to subhedral olivine phenocrysts with iddingsite alteration from the Longipi shield. (B) PPL image of olivine phenocrysts altered by bowlingite along fractures. (C) XPL image of a porphyritic-coarse grained sample from Longipi. Phenocrysts of olivine (extinct in image), plagioclase, and zone clinopyroxene are common in these samples. (D) PPL image of olivine and plagioclase phenocrysts from the Kulal shield. Note the smaller olivine phenocryst is completely altered, whereas the larger phenocryst exhibits alteration along rims and fractures. (E) PPL image showing flow alignment (direction shown by red arrows) in plagioclase laths in a Kulal shield sample. (F) XPL image of olivine aggregate from the Asie Shield. (G) PPL image of subhedral olivine crystals from Huri Hills. Note the alteration along rims and fractures. All scales are 500 microns except in D (200 microns) and E (2mm). cpx = clinopyroxene; ol = olivine.

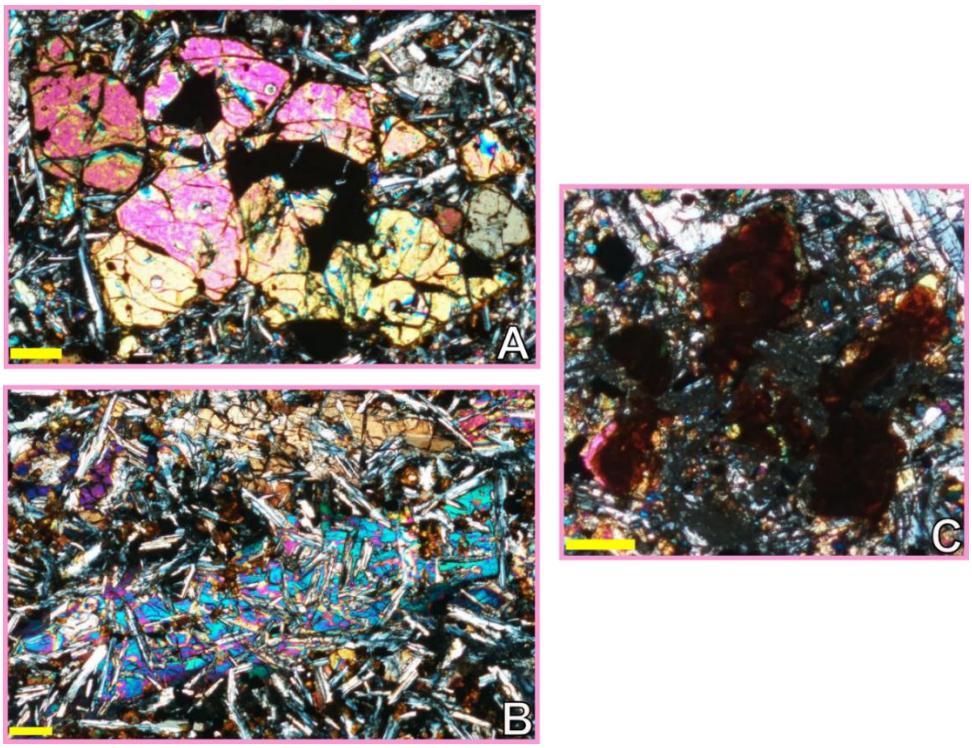

Figure 6. XPL petrography images of Kankam (A) Olivine cumulate in a Kankam basalt with intergranular groundmass. (B) Ophitic texture in a Kankam basalt, where thin plagioclase laths are enclosed by large, tabular clinopyroxene phenocrysts. (C) Olivine microphenocrysts in a microcrystalline sample that have been partially to completely altered by iddingsite. Scale = 500 microns in A and B; 200 microns in C.

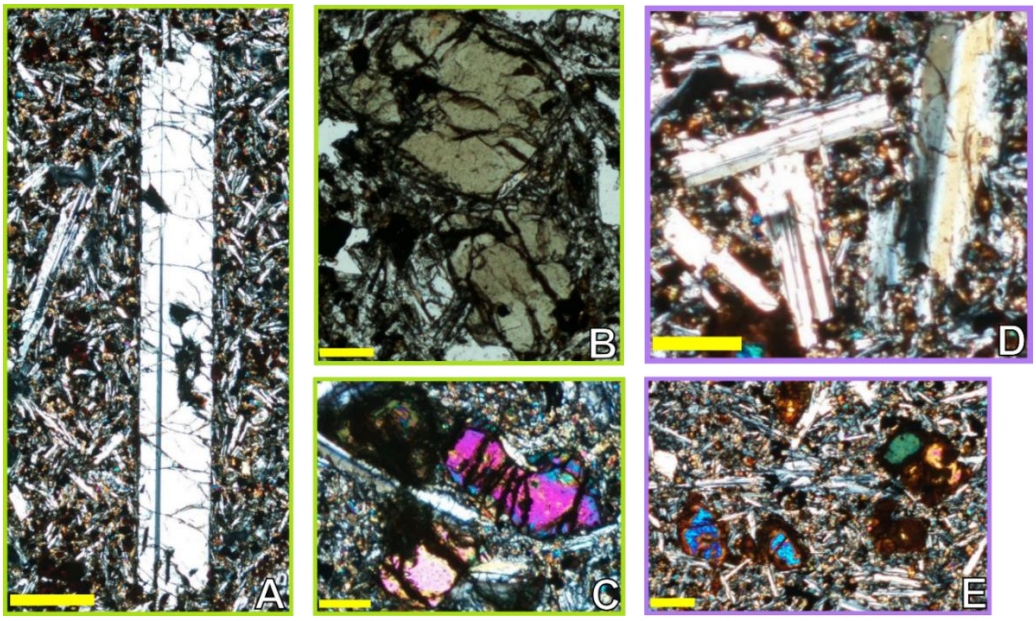

Figure 7. Petrography of Lenderit basalts (A-C) and Balo basalts (D-E). (A) XPL image of a large and tabular plagioclase phenocryst set in an intergranular groundmass. (B) PPL image of zoned clinpopyroxene phenocrysts from Lenderit. (C) XPL image of olivine microphenocrysts from Lenderit exhibiting alteration along fractures. (D) XPL image of twinned plagioclase phenocrysts from the Balo basalt. (E) XPL image of partially to completely altered olivine microphenocrysts from the Balo basalt. Scale: 500 microns in A; 200 microns in B-D and 250 microns in E.

Ta peak (Figure 9). There is also a small peak in Ba, a slope break between K-La, peaks in Sr and Nd, and a negative anomaly in P. Although the Th-U trough and Nb-Ta peak are present, the lack of a distinct Ba peak suggests that Asie deviates from the Type III magma pattern, resembling more of a Type IV pattern (Rooney, 2020d). In a chondrite normalized diagram, Asie shield is also characterized by higher concentrations of LREE relative to HREE, but compared to Longipi and Kulal, the pattern is overall less enriched (Figure 10).

Huri Hills: This sample exhibits a primitive composition (about ~10 wt. % MgO; see Figure 8). No major and trace element trends can be identified for Huri Hills, but we are able to describe its trace element pattern in primitive mantle normalized diagrams. The pattern for Huri Hills is characterized by large peaks in Ba and Sr, as well as a Nb-Ta peak and Th-U trough (Figure 9). Other characteristics of this pattern include small peaks in La and Nd, and negative anomalies in K, P and Ti. With the exception of the distinct Sr peak, Huri Hills exhibits a pattern that broadly represents Type III magmas. Chondrite normalized plots for Huri Hills shows a relative enrichment in LREE than HREE. This pattern is also overall more enriched than Asie. However, there is a distinct behavior in Tm-Lu, where the pattern is nearly horizontal in character. This is not displayed by any other group in our study (Figure 10).

Kankam Basalt: Out of the three lava flows correlated with the Pliocene shields, the Kankam basalts show the most compositional variability (Figure 8). These basalts are characterized by primitive compositions, as well as having the highest MgO (up to ~15 wt. %) from this phase. It is important to note, however, that the Kankam samples with high (>8 wt. %) MgO are those that contain olivine cumulates, thus, the accumulation of this phase has likely resulted in such high concentrations. Kankam basalts show an increase in major elements with decreasing MgO, with the exception of CaO (wt. %) and Al_2O_3 (wt. %), where concentrations of the latter begin to decrease at ~6 wt. % MgO. Overall, Kankam shows an increase in incompatible elements and a decrease in compatible elements with decreasing MgO (wt. %).

A distinct clustering of samples at ~6 wt. % MgO in major and trace element concentrations has been identified in the Kankam basalts. This clustering, however, is less pronounced in Sc and Rb concentrations (ppm). The Longipi shield sample with low MgO (wt. %) also plots within this Kankam cluster. The lack

of clustering behavior in Kankam samples with higher MgO (>8 wt. %) could be attributed to olivine accumulation, but because of the overall compositional variability within Kankam, it is also possible that the clustered samples are representative of the same lava flow.

Kankam exhibits Ba and Nb-Ta peaks as well as the U-Th trough in primitive mantle normalized diagrams (Figure 9), the latter being steeper in magmas with >8 wt. % MgO. These lavas also exhibit a K negative anomaly and a pronounced peak in Nd. Samples with ~6 wt. % MgO exhibit a negative anomaly in Ti, which is not identified in the more primitive samples of this group. In contrast, samples with >8 wt. % MgO have a pronounced Sr peak that is not found in lavas with ~6 wt. % MgO. Some samples also exhibit a slight Zr-Hf anomaly, which deviates from the magma Type III pattern. Despite these minor deviations, which could indicate contributions from other sources (see section 5.3.1 for details) this group broadly follows a magma Type III pattern (Rooney, 2020d). There are also distinct differences between the Kankam samples of ~6 wt. % MgO and higher MgO concentrations in chondrite normalized diagrams. Although there is an overall enrichment in LREE relative to HREE, the more primitive lavas of Kankam are less enriched in the LREE than those with ~6 wt. % MgO. Additionally, primitive samples show variation in the concentrations of LREE, while its concentrations eventually converge towards the HREE. This convergence is more pronounced in Ho-Lu (Figure 10).

Lenderit Basalts: Lenderit lavas exhibit the most evolved compositions of the shield building phase (Figure 8). These flows range between ~2-7.6 wt. % MgO and have the highest TiO_2 (3-3.5 wt. %) content out of all the groups of the shield volcanism phase. The data for Lenderit is scattered, making it difficult to establish trends in major and trace elements. However, they exhibit a decrease in Al_2O_3 (wt. %) and CaO (wt. %), Sr (ppm) and compatible trace elements as samples become more evolved, but an increase in REE and other incompatible trace element concentrations (ppm). Trace element patterns in primitive mantle normalized plots (Figure 9) show Ba and Nb-Ta peaks, negative K and Ti anomalies and, with the exception of one sample where the pattern is more flat, a Th-U trough. There is also a Nd peak exhibited by all the samples, but there is variability in some of the signatures for Sr, P where some samples exhibit a negative anomaly and others do not. There are also some samples that exhibit an anomaly in Zr-Hf similar to

Kankam. Despite these slight variations, Lenderit broadly follows a Type III magma pattern (Rooney, 2020d). Chondrite normalized diagrams of Lenderit show an overall enrichment in LREE relative to HREE, where one sample appears to be more depleted in HREE than the rest. Other characteristics identified include a slight peak in Eu for some samples (Figure 10).

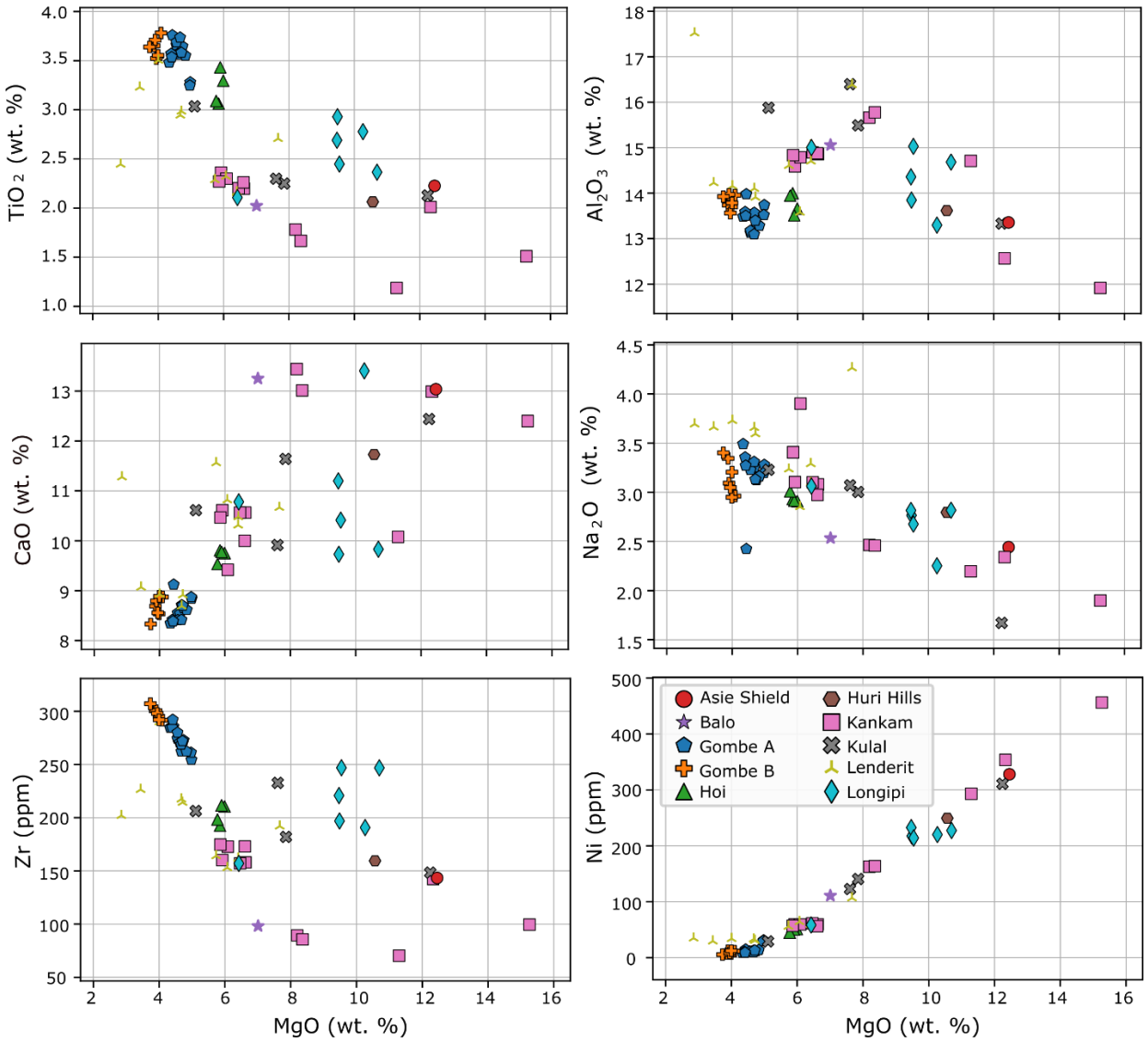

Figure 8. Selected major and trace element plots for the Gombe Stratoid Series and Pliocene shield groups. Note the overall compositional homogeneity of the Gombe Stratoid Series and the variable compositions of the Pliocene shields.

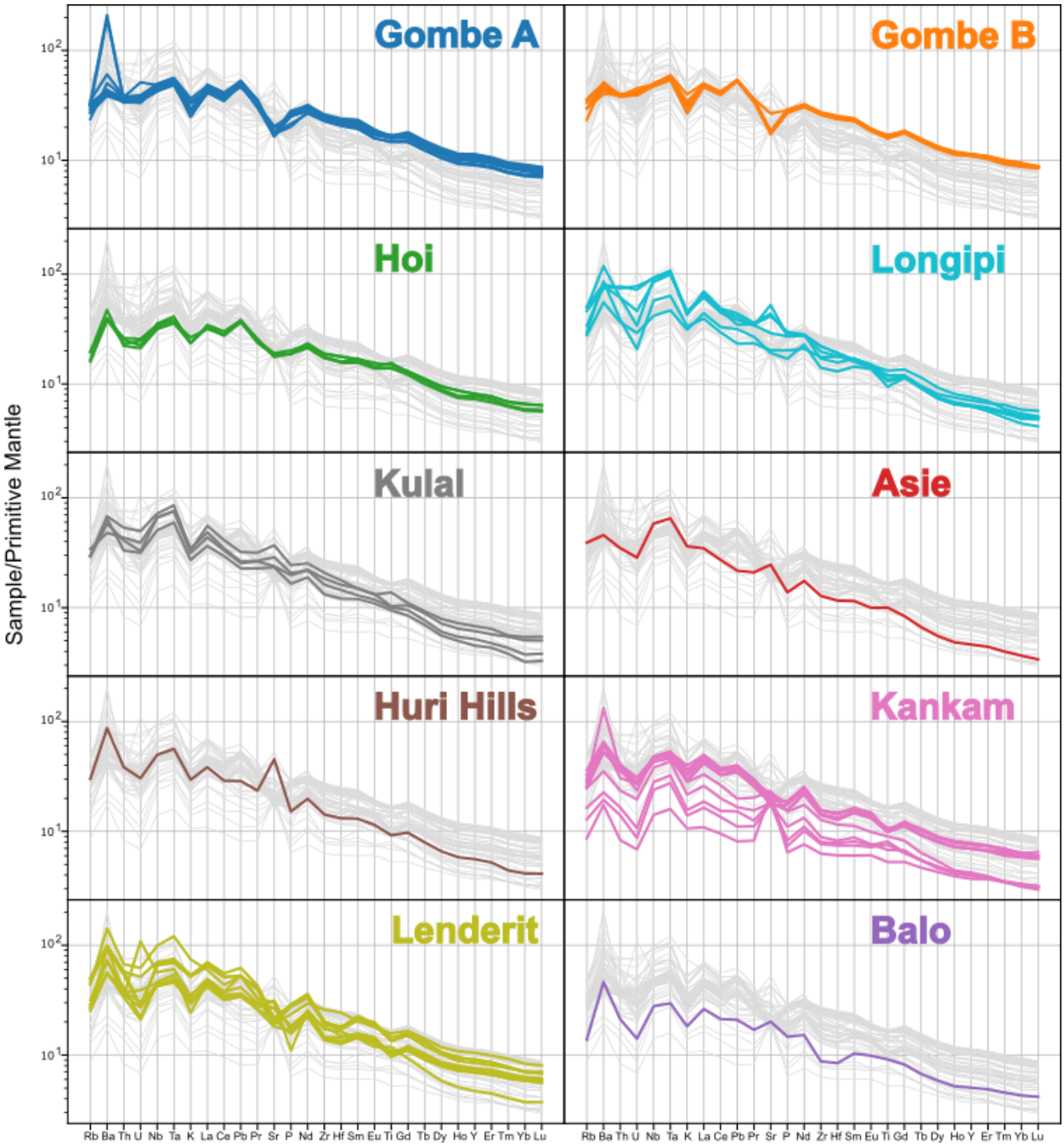

Figure 9. Primitive mantle normalized diagrams (Sun and McDonough, 1989) of the Gombe Stratoid Series groups and the Pliocene Shields.

Balo Basalt: Similar to Asie Shield and Huri Hills, we are unable to establish any trends for the Balo basalt, but this sample has a primitive composition (about 7 wt. % MgO) and plots between the low (~6 wt. %) and high (> 8 wt. %) MgO samples of Kankam (Figure 8). For the most part, this sample plots near the ~ 6 wt. % MgO Kankam samples, except for CaO, Na_2O and K_2O (wt. %), REE, Pb, Rb, Th, Ta and Hf (ppm),

for which the sample plots near the higher MgO (wt. %) Kankam samples. The Balo basalt's primitive mantle normalized pattern (Figure 9) shows a peak in Ba and Nb-Ta, K negative peak, and a Th-U trough. This sample follows a Type III magma pattern (Rooney, 2020d), however, similar to Kankam and Lenderit, there is a distinct Zr-Hf trough that is not characteristic of Type III. The chondrite normalized plot of Balo also shows an enrichment of LREE relative to HREE with a slight peak in Eu (Figure 10).

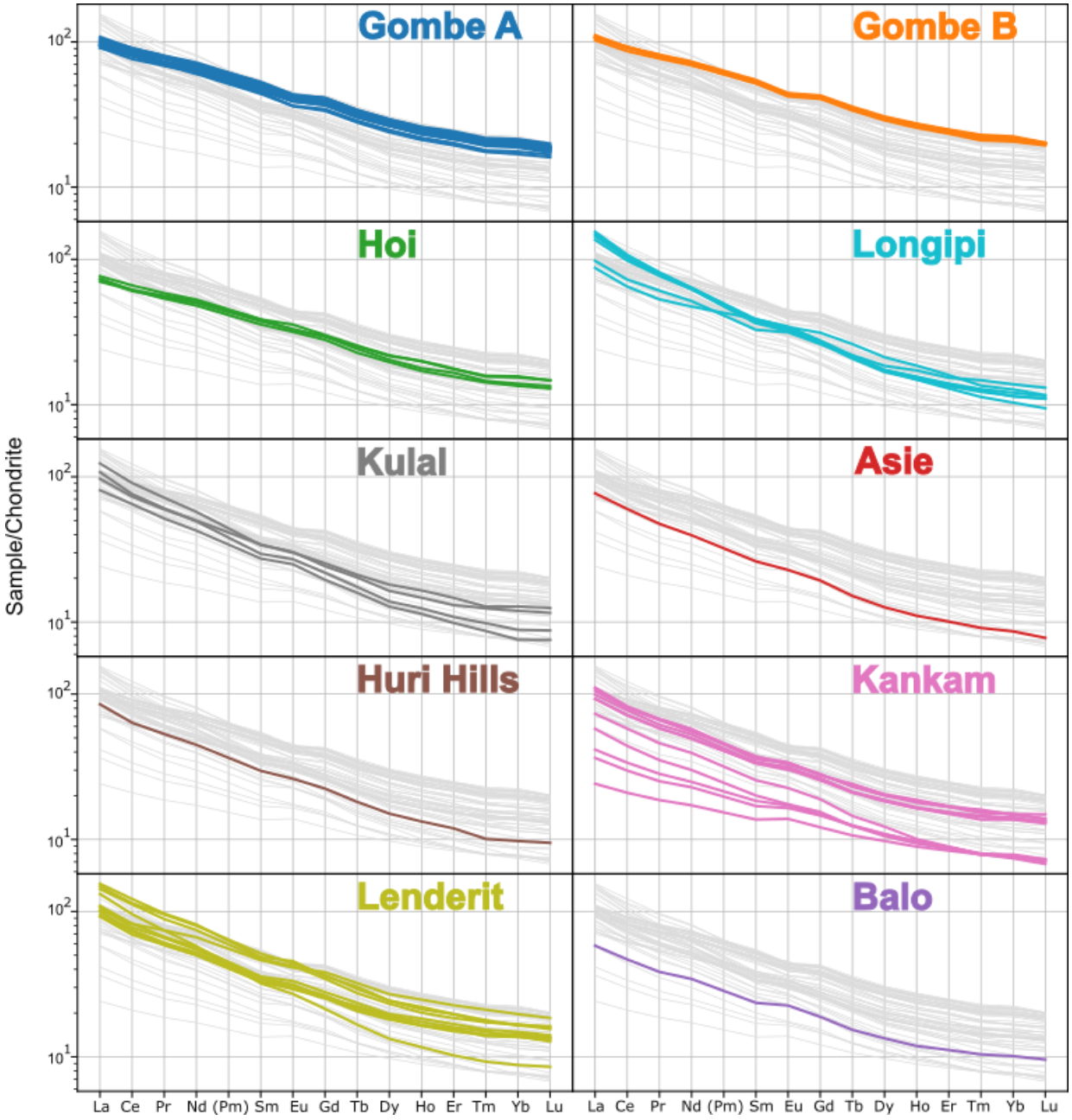

Figure 10. Chondrite normalized diagrams of the Gombe Stratoid Series groups and the Pliocene Shields.

5. Discussion

5.1. Similarities between Gombe and older flood basalts provinces within the EARS

The Gombe Stratoid Series has been described in previous studies as a flood basalt event (e.g., Bruhn et al., 2011; Feibel, 2011). Although these lavas are areally-extensive, their volume is estimated by Haileab et al. (2004) to be less than 5000 km^3, making this group significantly smaller in volume than previous flood basalt events within East Africa such as the ~24,000 km^3 Oligocene flood basalt volcanism in Turkana (Rooney, 2017) and the Ethiopian-Yemen flood basalts estimated at ~300,000 km^3 (see Corti, 2009 and references therein). Despite this, several characteristics of the Gombe Stratoid Series resemble those of flood basalt provinces, but at a much smaller scale:

Morphology: The Gombe Stratoid Series is a widespread, fissure eruptive event that is characterized by stratiform basaltic flows. Watkins (1986) suggested that the eruption of these lavas lasted about 2.5 Ma, however, Haileab et al. (2004) propose that most of the eruption of the Gombe Stratoid Series occurred in an interval of 0.3 Ma. These characteristics support a parallel between the Gombe Stratoid Series and continental flood basalts within the EARS, where fissure eruptions and short intervals are prominent. An example of such is the eruption of the Eocene-Oligocene flood basalts in Ethiopia, which dominantly occurred by fissures and in a time interval of less than 5 Ma (see Corti, 2009 and references therein). Furthermore, these flood basalts are plateau forming (e.g., Ethiopian and Somalian plateaus; Corti, 2009). Similarly, the Gombe Stratoid Series formed the Gombe and Suregei plateaus located East of Lake Turkana, as evidenced by extensive exposures of this group in these regions (e.g., Haileab et al., 2004).

Composition and petrography: The Gombe Stratoid Series is dominated by large volumes of evolved and compositionally homogenous lavas. Continental flood basalts rarely erupt primitive lavas and are instead dominated by moderately evolved lavas that require significant differentiation within the continental crust (Cox 1980; Villiger et al., 2004). The development of the trans-crustal magma differentiation systems necessary to fractionate the large volumes of magma entering the crust necessarily results in magma homogenization; magma fractions evolve in different parts of the system mix as melt transits the system and erupts lavas with limited compositional heterogeneity (e.g., Kieffer et al., 2004). This process of

differentiation within the crust – modelled as recharge, evacuation, assimilation, and fractional crystallization – shows distinct parallels between models constructed for the Gombe Stratoid Series (see section 5.2.2) and continental flood basalts (Steiner et al., 2022; Davis et al., 2022). In addition, there are important textural similarities between the Gombe Stratoid Series and continental flood basalts. In a petro-stratigraphic study of the Low-Ti flood basalt province in Ethiopia, Krans et al. (2018) identified the different textural groups including intergranular, microcrystalline, and glomerophyric textures. Although the mineral composition may not be the same – olivine is a main phase in this flood basalt province (see Krans et al., 2018) and not found in Gombe – we have identified these textures within the Gombe A and/or B lava groups.

Shield volcanism: An important parallel between the Pliocene Gombe Stratoid Series and the Eocene-Oligocene flood basalt phase is that both of these voluminous events were followed by less voluminous activity in the form of shield volcanoes emplaced on top of the widespread basaltic flows (e.g., Ayalew et al., 2002; Kieffer et al., 2004; Corti, 2009; Rooney, 2017; Rooney 2020a). It has been suggested that, on the basis of composition, the shield volcanoes that overlie the Ethiopian flood basalts represent a continuity in the magmatic system, but a decrease in the magmatic flux, (Kieffer et al., 2004; Rooney, 2017). We propose a parallel process for the Gombe Stratoid Series where there is a transition from stratiform basalts to Pliocene shield volcanoes. Both the Gombe Stratoid Series and subsequent shields dominantly exhibit the same magma patterns (Type III), requiring a continuity in the mantle sources contributing to magmatism. Moreover, the more mafic composition of the Pliocene shield volcano lavas implies a less efficient magma plumbing and homogenization system in comparison to the earlier Gombe Stratoid lavas.

5.2. Constraints on the origins and formation of the Gombe Stratoid Series

Although the similarities between the Gombe Stratoid Series and continental flood basalts are evident, it is also important to highlight the vast differences in scale between these events. Said difference requires an examination of the mechanisms involved in melt generation. Continental flood basalts, such as those within the EARS, are suggested to have been generated as the result of the interaction between extension and plume material, resulting in decompression melting of the latter (e.g., Rooney, 2017). The magmatism

that followed these initial events (ca. 20 Ma onwards) shows a strong correlation with rift evolution, and is thus suggested to result from the lithospheric thinning processes within the rift (Rooney, 2017). To determine the mechanisms of melt generation, we first need constraints on the melting and equilibrating conditions of the magma source, including mantle potential temperatures (T_p), pressure, and depth.

5.2.1. Mantle Potential Temperatures and Source Modelling

Trace element patterns of the Gombe Stratoid Series are dominated by a Type III magma pattern; such magmas are derived from the asthenosphere and are considered to be a mixture between detached African lithosphere, plume material, and depleted mantle (Rooney 2017, 2020d; Rooney et al., 2012b). Determining the temperature and depth of melt equilibration is a key step to understand how these components were combined to generate the composition of the melt. Due to the absence of primitive (>6 wt. % MgO) compositions in the Gombe Stratoid Series, we constrain these parameters using primitive compositions from the Pliocene shield volcanism that followed the Gombe Stratoid Series that also exhibit a Type III signature.

5.2.1.1. Melt Equilibration and Mantle Potential Temperatures Results

To determine the conditions at which the melt was equilibrated in the mantle, we used the Si-Mg thermobarometer of Lee et al. (2009) and compared the results to the major element models of the Hydrous Adiabatic Mantle Melting Simulator (HAMMS; Kimura and Kawabata, 2014). The Lee et al. (2009) major element model uses the Si and Mg content of the magmas to estimate these parameters. This SiO_2-based barometer, as explained by the authors, is less sensitive to mantle composition variations due to the buffering of silica at given P-T conditions based on the system's mineralogy. Samples from the Pliocene shield volcanoes were chosen on the basis of composition (e.g., MgO > 6 wt. %) and mineralogy; lavas that exhibited olivine accumulation were not modelled. Because this thermobarometer requires primary magma compositions, samples where fractionation of olivine was accompanied by the fractionation of plagioclase and clinopyroxene were back corrected for primary compositions using the Petrolog v.3.1.1.3 modeling suite of Danyushevsky and Plechov (2011) following the methods discussed in Abu El-Rus and Rooney (2017) and Chiasera et al. (2021). In contrast, samples which only exhibited olivine fractionation were back

corrected to primary compositions using the olivine built-in correction on the Lee et al. (2009) thermobarometer. Model constraints were chosen following the parameters detailed in Appendix B of Brown et al. (2022): Fo = 89.5, $K_D^{ol\text{-}liquid}$ = 0.34 and Fe_{total} = 0.15.

Resulting melt equilibrium pressure conditions from the Lee et al. (2009) thermobarometry model range from 1.33-2.96 GPa, while temperature ranges from 1313-1487 °C. Using the pressure results, we estimated the depth of these equilibrated melts, resulting in a range from 40-89 km (see Table 3). For a direct comparison with the major element results from HAMMS, the temperature results from Lee et al. (2009) were converted into mantle potential temperatures (T_p). This also allows us to determine if the melt that produced these magmas was generated by the elevated mantle potential temperatures previously identified within East Africa (e.g., Rooney 2012c). To convert T to T_p, the equations of Putirka (2016) were used (Equations 12a-c and 14a-c). The resulting mantle potential temperatures from the major element modeling range from 1295-1448 °C. In contrast, T_p results from the HAMMS major element model range from 1333-1482 °C, which are 26-47 °C higher than those from the Lee et al. (2009) model.

5.2.1.2. Determining the melting conditions of the source

To determine the conditions at which the melt was generated in the mantle, the HAMMS trace element model (Kimura and Kawabata, 2014) was used. The sensitivity of incompatible trace elements to mantle melting aids in constraining the source composition and estimating the melting parameters (see Kimura and Kawabata, 2014 and references therein). HAMMS is a forward model that can estimate the parameters involved in melt generation: mantle potential temperature (T_p), water content, pressure (P), source depletion (CsDep), and source contamination (F_{cont}) (Kimura and Kawabata, 2014). Given that we have identified Type III magmas in our samples, several lithologies (i.e., depleted mantle, African lithosphere, plume material; Rooney, 2020d) are involved in generating these magmas. For this reason, we have followed the procedure detailed in Chiasera et al. (2021) to establish the source melt and contaminant lithologies to use in HAMMS.

Table 3. Major and Trace element thermobarometer results.

Sample (IGSN)	TOR0000O1	TOR0001D8	TOR0001D9	TOR0001DK	TOR0001DL	TOR0001DP
T (°C) major elements (Lee et al. 2009)	1313	1485	1463	1325	1487	1444
P (GPa) major elements (Lee et al. 2009)	1.33	2.72	2.56	1.58	2.96	2.48
Calculated depth (km)	40.0	81.7	76.7	47.5	88.9	74.5
Calculated Tp (°C)	1295	1448	1429	1303	1448	1411
Tp (°C) major elements (HAMMS)	1333	1474	1475	1334	1482	1458
P (GPa) major elements (HAMMS)	1.29	2.72	2.36	1.94	2.87	2.43
Tp (°C) trace elements (HAMMS)	1410	1422	1412	1411	1418	N/A
Pressure (GPa) trace elements	2.98	3.15	3	3.03	3.15	N/A
H2O content (wt. %)	0.1	0.1	0	0	0.1	N/A
CsDep	1	0.1	0.2	0.5	0.2	N/A
Fcont	0.9	0.7	0.5	0.4	0.2	N/A
Calculated depth (km) from trace	89.4	94.5	90	90.9	94.5	N/A

For these models, we used all of the samples used in the Lee et al. (2009) thermobarometry model except for one (TOR0001DP), as this sample deviates from the magma Type III pattern by having signatures more representative of Type IV magmas (see section 5.2.4 for details). Because this magma type is a hybrid composition (see Rooney, 2020d for details), the HAMMS model is not able to reproduce the source melt. We tested our samples in a T_p range of 1400-1450 °C, P range of 2.9-3.2 GPa, H_2O content from 0-0.5 (wt. %), and both source depletion (CsDep) and source contamination (F_{cont}) ranging from 0-1. The conditions that best match our samples are the following: T_p = 1410-1422 °C, P = 2.98-3.15 GPa, CsDep = 0.1-1.0 and F_{cont} = 0.2-0.9. Using the pressure results, the estimates of the depth in which these melts were generated range from about 89 – 95 km (see Table 3).

5.2.1.3. Implications

The results of trace element source models indicate that the initial melting of the parent melt of these

magmas occurred at a depth of ~89-95 km with T_p = 1410-1425 °C. In contrast, these melts equilibrated at shallower depths ranging from 40-89 km, with differing major element T_p ranges between the two major element models. It is important to note that two samples exhibited cooler T_p than the rest: TOR0000O1 and TOR00001DK (see Table 3), both from the Longipi Shield. Despite these samples exhibiting cooler temperatures than the rest, elevated mantle potential temperatures are evident in both the initial conditions of melt as well as melt equilibration. These elevated mantle temperatures indicate that plume material plays a role in the generation of Type III magmas in Turkana.

5.2.2. Recharge, Fractional Crystallization (RFC) Model of the Gombe Stratoid Series

Magma plumbing systems of continental flood basalt provinces are typically complex (e.g., Steiner et al., 2022). The processes in which these magmas differentiate within the plumbing system involve recharge, assimilation, and fractional crystallization occurring within the crust prior to eruption (Steiner et al., 2022; Davis et al., 2022). The Gombe Stratoid Series shows compositional homogeneity and limited MgO concentrations, which is indicative that significant differentiation had to occur before these lavas erupted. Given the compositional and textural similarities between the Gombe Stratoid Series and continental flood basalts, we explore whether a complex magma plumbing system is necessary to generate the Gombe Stratoid lavas.

5.2.2.1. Justifications for the Model

Magmatic differentiation of the Gombe Stratoid Series: We have shown that the samples from the Gombe Stratoid Series are characterized by broadly homogeneous and moderately evolved compositions, with an overall enrichment in incompatible trace elements as MgO decreases. Lack of primary magmas in the Gombe Stratoid Series implies that magmatic differentiation occurred prior to eruption. Fractional crystallization is one of the processes in which magmas differentiate, but considering the limited variability of MgO concentrations in Gombe, this process alone cannot account for a composition that has likely reached a steady state (Lee et al., 2014; see also O'Hara and Mathews, 1981). In contrast, in a system where fractional crystallization is accompanied by magma recharge, MgO concentrations will not exhibit large variation; although this element is favored in the solid phase, the addition of new, more primitive

compositions into the magma chamber will result in compositions that are less varied (e.g., Lee et al., 2014). Although fractional crystallization will result in enrichment of incompatible trace elements in the melt, Lee et al. (2014) explains that these concentrations will be higher in a system that undergoes fractional crystallization and magma recharge rather than fractional crystallization only. We thus explore whether a combination of these processes results in the homogeneous compositions exhibited by the Gombe Stratoid Series.

Hoi Basalt – potential precursor event of the Gombe Stratoid Series: The sudden large-volume and widespread volcanism of evolved basaltic compositions after a period of significant quiescence in Turkana is an unusual feature of the Gombe Stratoid Series. A potential precursor of this event may be represented by the Hoi basalt, a basaltic unit informally named by Bruhn et al. (2011) that is located within the KSFB/Gombe Plateau. No specific age data is available for this unit, but Bruhn et al. (2011) suggest that it is older than the Gombe lavas based on locality and the compositional differences between them. Our geochemical results show that despite sharing some similarities (e.g., Al_2O_3, high TiO_2), the Hoi basalt is different in composition than Gombe. This basaltic unit is characterized by higher MgO, enrichment in compatible elements and depletion in incompatible elements relative to Gombe, indicating that Hoi is less differentiated than the former. Considering the magmatic hiatus before the Gombe Stratoid Series, there are two possibilities that could explain the origin of the Hoi basalt: a) this basaltic unit is a part of the Miocene volcanism recorded before the period of quiescence or b) Hoi is representative of a primitive-endmember within the Gombe system that erupted prior to the Gombe A and B lava groups. A geochemical comparison between the Hoi basalt and Miocene rocks from the region (i.e., Turkana, Kenya, and Ethiopia) shows no apparent relationship between Hoi and volcanic activity from this time, making them unlikely to be Miocene in age (Figure 11). In contrast, the geochemistry of Hoi and the Gombe Groups show a more apparent trend between the groups, where Hoi appears to represent a less differentiated member of the Gombe Stratoid Series. Based on these observations, we hypothesize that the Hoi basalt is a unit representative of a primitive endmember of Gombe whose eruption preceded the "main" Gombe (Gombe A and B) eruption.

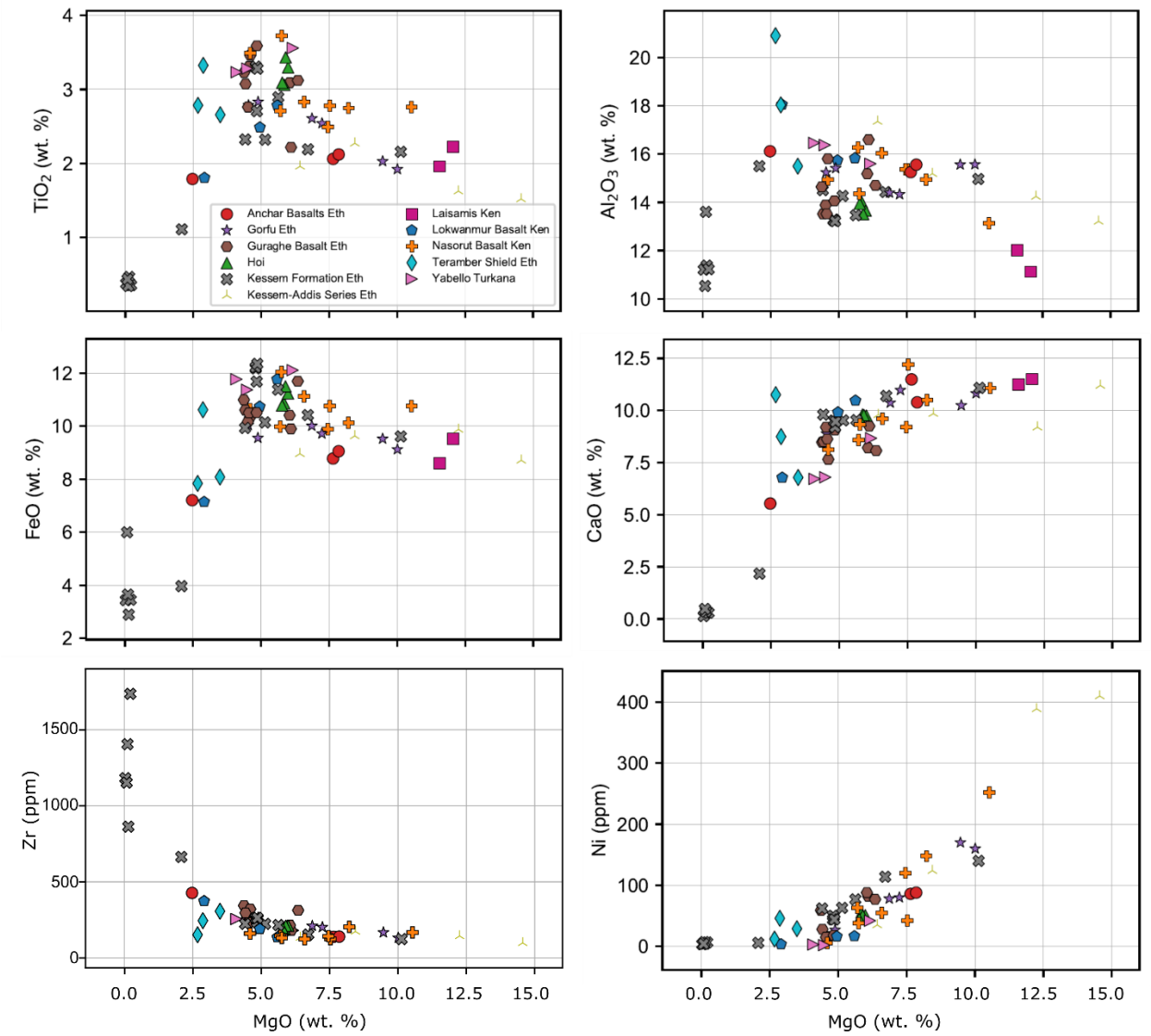

Figure 11. Selected major and trace element data of the comparison between the Hoi Basalt with Miocene volcanism in Turkana, Ethiopia (Eth) and Kenya (Ken). Data collated by Rooney (2020a).

5.2.2.2. RFC Model Results

Given the overall homogeneity of the Gombe Group, we have conducted a recharge, fractional crystallization (RFC) model using Magma Chamber Simulator (MCS; Bohrson et al., 2014) to constrain the magma differentiation processes in the system causing this homogeneity. MCS is a thermodynamic model that incorporates energy constrained (EC) RAFC models (see Bohrson et al. 2014 and references therein) and rhyolite-MELTS (e.g., Gualda et al., 2012) to obtain the conditions of an open system undergoing processes such as fractional crystallization, RFC, among others, as it evolves. This model works with a series of sub-systems (e.g., Magma, Recharge, Wall rock) for which the user inputs their

composition, temperature, and mass, as well as initial pressure and fO_2 conditions of the magma body (Bohrson et al., 2014). For Gombe, we have opted for an RFC-only run, given we currently lack evidence for significant assimilation of the crust. These models were tested using both major and trace element concentrations of Gombe lavas. The compatible elements Cr, Ni, and Sr were chosen for our models as they partition into pyroxene, olivine, and plagioclase, respectively. We also included the incompatible elements Nb and La to our models. Nb is sensitive to Fe-Ti oxides, whereas La serves as a probe for incompatible behavior at low MgO (wt. %) concentrations. To maintain a consistent dataset for magmatism within East Africa, partition coefficients used in these models follow those used by Steiner et al. (2022) in their study of Eocene flood basalt volcanism in Ethiopia and Kenya.

Based on our hypothesis that the Hoi lavas are a precursor to Gombe, we have explored whether the Gombe Groups (A and B) can be derived from a Hoi composition through RFC processes occurring within the crust. For our models, we used Hoi sample TOR0000OV as the composition for the initial magma as well as all recharge events. This sample was chosen on the basis of being the most primitive of the Hoi lavas in our suite and due to its TiO_2 and Al_2O_3 concentrations that encapsulate the concentrations of the Gombe Groups. Although MgO concentrations of the Hoi lavas do not show any significant variation (e.g., all within 5.7-5.9 wt. %), they do exhibit slight variation in other major elements, resulting in either too high or too low values for modeling Gombe.

Our results show that RFC processes with a Hoi composition replenishing the magma chamber can produce the Gombe compositions at different pressure conditions in the upper crust, further indicating that the Gombe Stratoid Series is representative of a high flux magmatic event. Gombe A group is produced at 1-2 kbar, whereas Gombe B group is produced at 3 kbar (Figure 12). However, there is a pronounced deviation in our models for Gombe B group with respect to CaO (wt. %) and Na_2O (wt. %). At 3 kbar, recharge results in low CaO (<8.5 wt. %) and high Na_2O (>3.5 wt. %). Increasing the mass of the recharge events (e.g., from 10 grams to 30 grams) only broadens the range in which the recharge events occur, but does not increase or decrease the elemental concentrations of the events, providing no solution to this discrepancy. We thus suggest that the deviation in CaO and Na_2O can be attributed to the effect of the

glomerocrysts in the major and trace element concentrations of the Gombe B lavas (noted in section 4.1). As previously explained, accumulation of pyroxene and plagioclase, will increase the CaO concentrations and decrease Na_2O concentrations in the bulk rock compositions.

RFC models are also in agreement with the trace element concentrations of the Gombe Group. However, it is important to note that the partition coefficients from Steiner et al. (2022) overestimate some of the trace elements: Cr (Gombe B only), Ni, and Sr. While the overestimates of Cr and Ni (both about ~18 ppm higher) are still within error, Sr is overestimated by about 50 ppm. We tested a Sr partition coefficient for plagioclase of 2.87 (Higuchi and Nagasawa, 1969) available in the GERM database (https://kdd.earthref.org/KdD/); this value resulted in a better fit to our data (Figure 12f) than the 1.83 partition coefficient value used by Steiner et al. (2022). Partition coefficients are controlled by a number of factors, including pressure and temperature (see Rollinson, 1993). Higher partition coefficients are common as pressure increases (e.g., Rollinson, 1993 and references therein; Sun et al., 2017), however, our RFC models occur at shallow pressures (1-3kbar), for which a higher partition coefficient would not be reasonable. An increase in temperature may decrease the partition coefficients (e.g., Dunn, 1987), but oftentimes it is difficult to determine whether it is being affected by melt composition or temperature (see Rollinson, 1993 and references therein). Given that Sr partitions into plagioclase, it is possible that the overestimation of our data is due to not having enough fractionation of plagioclase in the system. If this is the case, using a different composition for the starting magma and recharge events may result in a better fit without having to use a higher partition coefficient. Further work is required to determine whether a different composition from the Hoi basalts will provide better results in our RFC models.

5.2.2.3. Implications

Lateral Migration of the system: Limitations exist when trying to accurately constrain the migration of the Hoi-Gombe magmatic system/s through time. It is difficult to determine if both Gombe A and B erupted simultaneously, or if Gombe A erupted prior to Gombe B. If we assume the latter, using the localities of the samples, the Hoi-Gombe magmatic systems could have initiated in or close to the Gombe Plateau, migrating westward through time (Figure 13). However, this is contradictory to the strain and rift migration

data in the Turkana Depression during this time period. Stratigraphic and age constraints of individual Gombe lava flows are required to effectively establish the evolution and possible migration of the magmatic system through time.

Trans-crustal magma differentiation: The results of our RFC models suggest that Gombe lavas were differentiated by RFC processes at different conditions in the upper crust, with the existence of shallow (~3.5-7 km) and deeper (~10.5 km) magma chamber systems based on pressure conditions of 1-2 kbar and 3 kbar respectively. Our models further support a relationship between Hoi and Gombe, as a composition of the former is able to successfully produce both Gombe groups by RFC processes The overall composition and textures of the Hoi Basalts (see section 4.1) suggests that they originated in a deeper chamber (>10.5 km) than Gombe lavas, differentiated via fractional crystallization processes, and likely stalled in the crust for a short period of time prior to eruption, as suggested by the presence of cotectic crystallization (Fig 14a).

Integrated model: Lavas from Gombe A are produced at low pressures (1-2 kbar) as indicated by our RFC models (see previous section). These low pressure conditions are also supported by the petrography of these lavas, in which plagioclase is the main phenocryst phase and cotectic crystallization of plagioclase and clinopyroxene occurs, providing evidence for a shallow system. Considering that Hoi likely stalled in the crust prior to eruption, we propose that Gombe A lavas formed in Hoi's former shallow chamber, and because larger degrees of melt were being produced, Gombe A stalled in the crust for longer, allowing for recharge and homogenization in this shallow chamber to occur (Fig 14b). In contrast, our RFC models show that Gombe B lavas were formed at slightly higher pressures (3 kbar), indicating the presence of a deeper chamber (about 10.5 km) than Gombe A. We are unable to determine if this chamber was active at the same time as Gombe A, but based on the more evolved composition of Gombe B, it is also possible for this chamber to have formed at a later time as the magmatic system migrated (Fig 14c). Although both Gombe groups have glomerocrysts and that bow-tie plagioclase is seen in these glomerocrysts, it is unlikely that

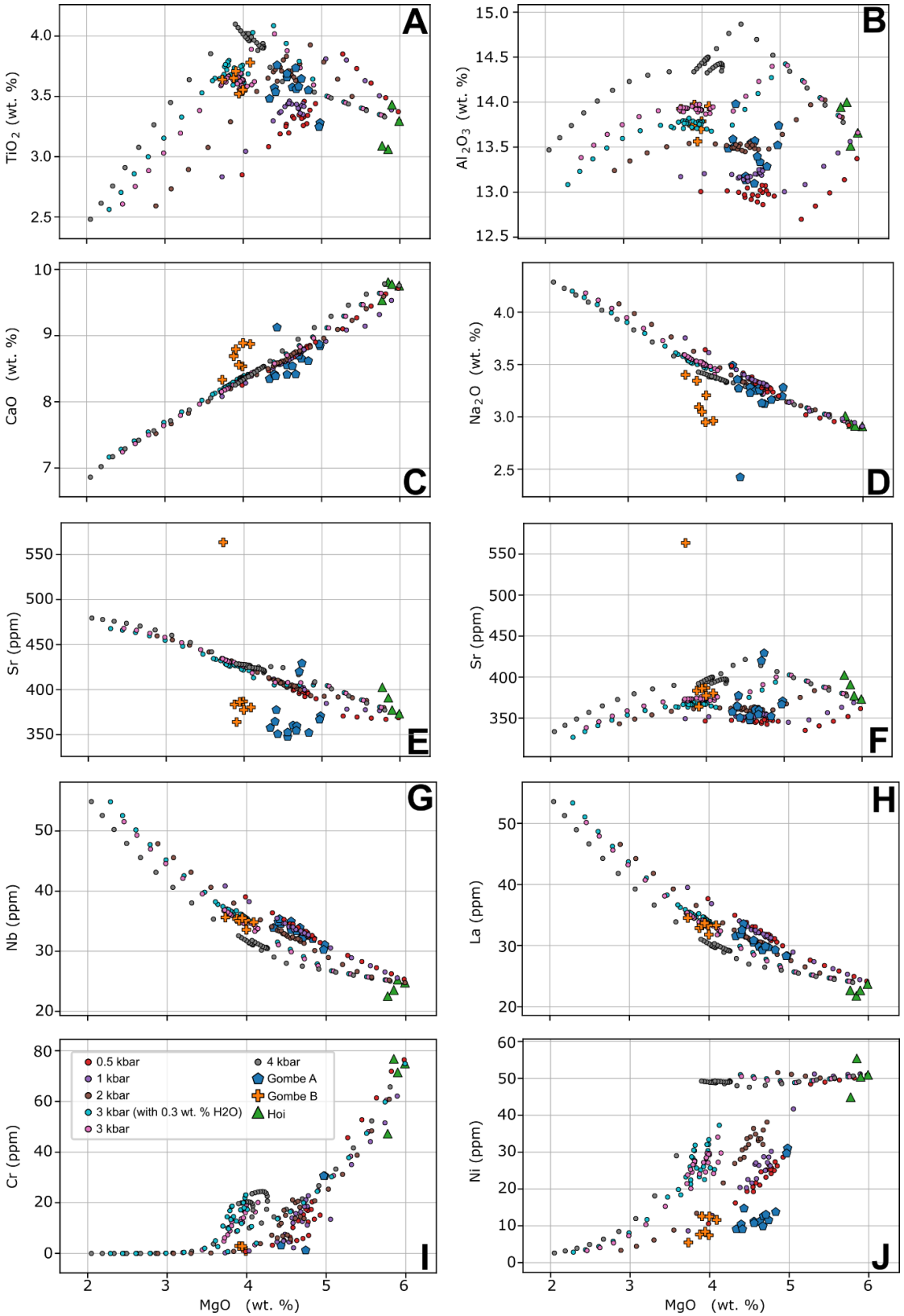

Figure 12. RFC modelling results from the Gombe Stratoid Series. A total of 10 recharge events of 10g each were used in each RFC run. We added 0.3-0.35 wt. % H_2O to our initial magma and recharge events composition and ran it through a range of pressures from 0.5 kbar to 4 kbar with FMQ set as the oxygen

Figure 12 (cont'd)
buffer. Due to the addition of H_2O in our magma and recharge compositions, MELTS v. 1.2.0 was used to run MCS. All runs with 0.35 wt. % H_2O in the starting magma and recharge magma compositions except where otherwise stated. Note the deviation of the models in (C) CaO (wt. %) and (D) Na_2O (wt. %). (E) Sr model results when using partition coefficients of Steiner et al. (2022). (F) Sr results when using a higher partition coefficient from Higuchi and Nagasawa (1969).

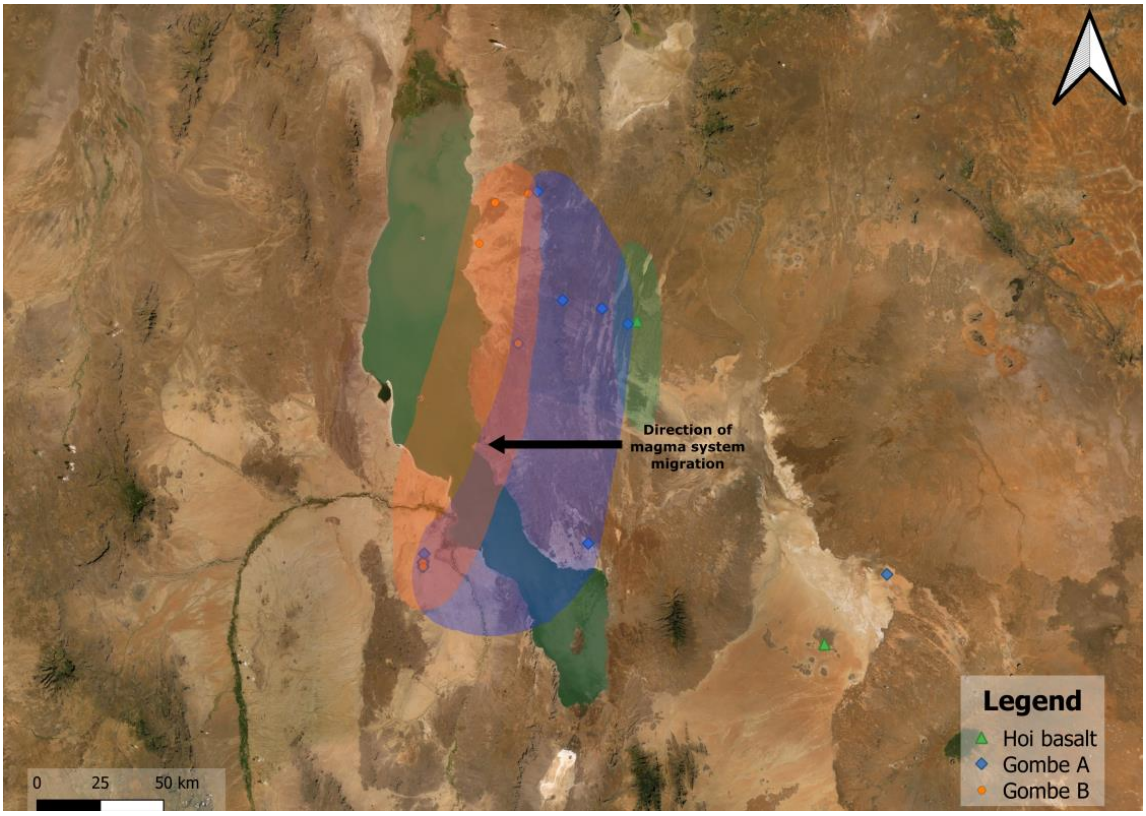

Figure 13. Magma system migration (~westwards) through time based on sample locality. This is opposite from the overall eastward migration direction of strain and rifting through time.

Gombe A and Gombe B were once part of the same magmatic chamber, instead, glomerocrysts likely formed at both chambers. The absence of cotectic crystallization in the Gombe B group (with the exception of one sample) suggests that this group likely did not stall in the crust, and if it did, it was not to the same extent as Gombe A.

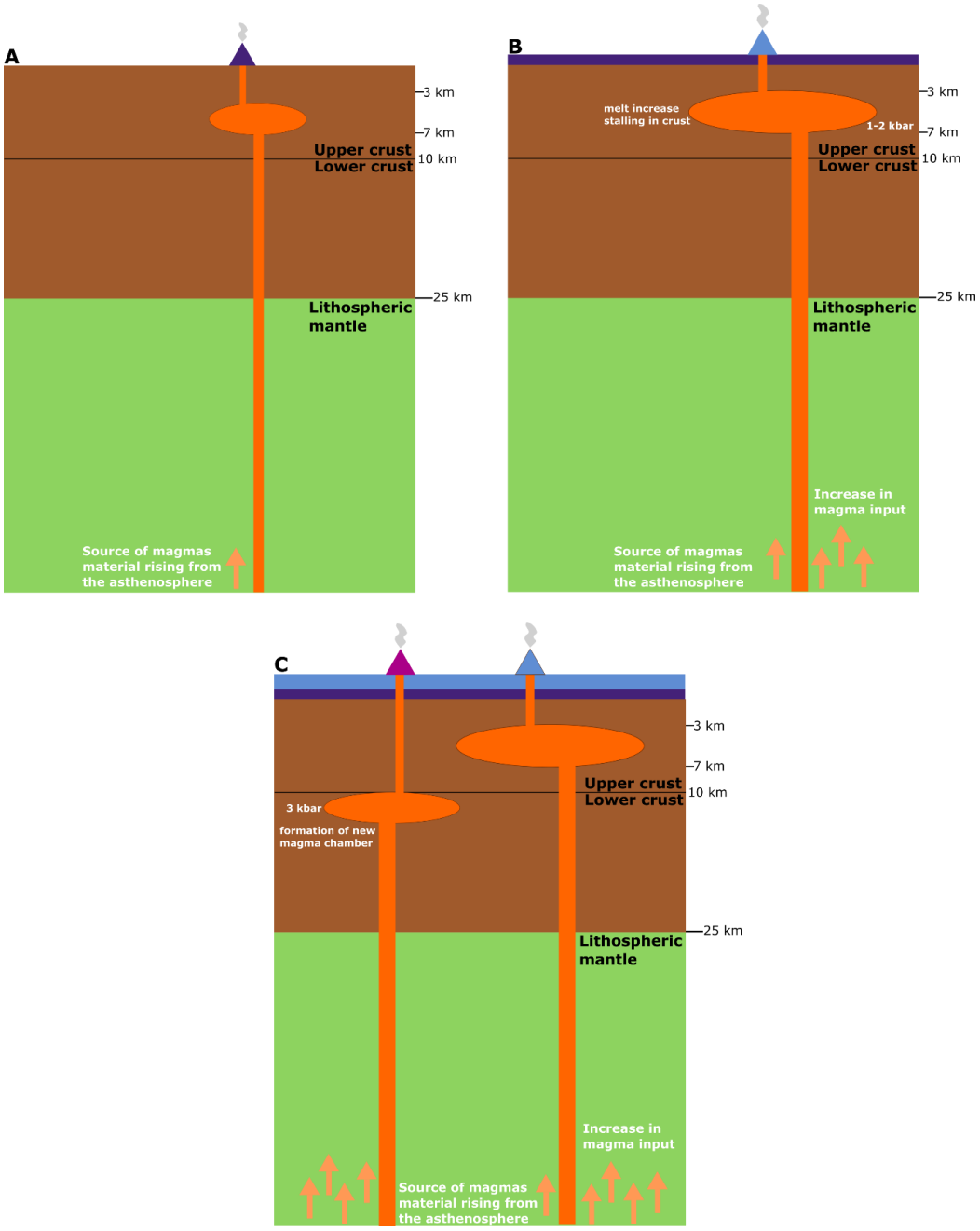

Figure 14. Evolution of the Gombe magmatic system through time (A) Eruption of the Hoi basalt is a precursor to the eruption of Gombe A and B. Hoi likely differentiated by fractional crystallization and stalled in the crust for a short period of time prior to eruption (cotectic crystallization present). (B) Beginning of the "main" Gombe eruption, likely starting with Gombe A as melt increased as a result of plate stretching. This group stalled in the crust for longer and differentiated via recharge of a Hoi composition as well as fractional crystallization. (C) A continuation of melt production due to plate stretching gives way to the formation of a new, deeper chamber where Gombe B is differentiated. This chamber is rich in glomerocrysts and likely did not stall in the crust prior to eruption. It is possible that both Gombe Groups erupted simultaneously (shown here), but another possibility is that Gombe B erupted after Gombe A. Detailed stratigraphy and age data for individual Gombe flows are needed to accurately constrain the evolution of the system. Depths estimations based on RFC model results. For details on the boundary between upper and lower crust in Turkana, see Rooney et al. (2022) and references therein.

5.3 Rifting, Magmatism, and the continental lithosphere – the origin of the Gombe Stratoid and Shield phases

Magmatic activity recorded in the Turkana Depression between the Pliocene-Recent is characterized by an initial period of widespread volcanism followed by volcanism in the form of shield volcanoes, eventually transitioning to focused axial magmatism in modern times (Rooney, 2020a). A magmatic period of similar magnitude and age has also been recognized in the Afar Depression (Rooney, 2020c). However, there is a significant difference between the activity in these two localities: In Afar, focused magmatism is emplaced on top of the preceding widespread event, whereas in Turkana, focused volcanic activity is located within Lake Turkana, away from where the initial widespread volcanism took place (see Rooney 2020a, 2020c). The behavior of magmatic activity in Turkana is therefore unusual; movement of magmatism away from the area expected to be most affected by extensional processes is not anticipated in rifting models (e.g., Corti, 2009). The causes of the observed migration of magmatism towards Lake Turkana and the link between magmatism and rifting activity remains an area of active research (e.g., Muirhead et al., 2022; Rooney et al., 2022).

The widespread Gombe Stratoid Series exhibits characteristics of a high flux event, as evidenced by the complex magmatic plumbing system in which these magmas differentiated by RFC processes. In order to generate high flux magmatic events, a high magma supply entering the plumbing system is required. One way of achieving higher magma flux is by decompression and melting of plume-derived material (e.g., Rooney, 2017), resulting in lavas that have high T_P (>1500°C). The initial Cenozoic magmatic events in East Africa formed the Eocene and Oligocene flood basalts, which have the highest recorded T_P of any lavas in East Africa (up to 1520°C: Rooney et al., 2012c). Mantle potential temperatures in our samples (1410-1422°C), while typically above ambient mantle values (i.e., T_P ~1350°C), are significantly less than those exhibited by the Oligocene and Eocene continental flood basalts. If the Gombe Stratoid Series was not generated solely by decompression of anomalously hot plume material, an important question arises: How can widespread volcanic events that resemble flood basalt volcanism, but at a miniature scale, be generated?

The observation of a transition from widespread flood basalts during the Eocene/Oligocene towards rift-focused magmatism during the Miocene and younger has prompted a model whereby the more recent magmatism in East Africa is controlled not by a plume but by rifting processes (Rooney 2017). In continental rift systems, extensional strain manifests as thinning of the continental lithosphere (e.g., Ebinger, 2005). To compensate for this thinning, material from the asthenosphere ascends, resulting in decompression melting and the formation of rift magmas (Ebinger, 2005). The Gombe Stratoid Series has been previously suggested to have resulted from an increase in tectonic activity by Haileab et al. (2004). This observation is in agreement with the increase in tectonic activity noted by Purcell (2018) to have occurred during the Pliocene in Turkana, likely due to changes in stress. These events resulted in the acceleration of rifting in the Lake Turkana basins, causing downfaulting in the Suguta region south of Lake Turkana (Purcell, 2018), and for several rifts in the region to experience maximum subsidence (Macgregor, 2015). Strain during the Pliocene was accommodated in the Lake Turkana basins, although rifting was still active in the Kerio basin (Vetel and LeGall, 2006; Muirhead et al., 2022; see Figure 2 for basin location). Vetel and LeGall (2006) also note a change in extension direction, which rotated North-East from its former East-West configuration. The Gombe Stratoid Series is also contemporaneous with the development of the Kino Sogo Fault Belt (KSFB; Figure 2), which reinforced the overall eastwards migration of strain (Vetel et al., 2005; Vetel and LeGall, 2006). This fault system cuts through the Gombe Plateau and connects the Chew Bahir Basin in the North to the Suguta basin in the South (Vetel and LeGall, 2006; Figure 2). The colocation between one of the main exposures of the Gombe Stratoid Series and the KSFB suggests that this region was among the most tectonically active during the Pliocene, resulting in widespread volcanism driven by lithospheric thinning. We have shown that T_p in lavas erupted during the Gombe Stratoid Series is elevated, consistent with the widespread presence of plume material throughout the East African mantle (e.g., Rooney 2020d), but is not elevated to the same level as that during the initial flood basalt phase. Additionally, the signatures exhibited by the Gombe Stratoid Series lavas (e.g., Type III) are ubiquitous within mature rifts in East Africa (e.g., Rooney, 2020d; see following section), therefore it is not surprising to see this signature during widespread magmatism, where large volumes of magma are being generated. It

is important to note, however, that in order to generate the large amounts of magma that erupted during the Gombe Stratoid Series, large portions of the lithosphere needed to be stretched so that enough asthenosphere could rise and undergo decompression melting. This observation implies that strain was likely distributed over a wide region. The findings of the aforementioned studies further support this implication, as we see that rifting was not only occurring in the KSFB/Gombe Plateau, but throughout several basins within Turkana. Thus, the findings of this study, combined with the wide distribution of strain throughout Turkana during the Pliocene suggest that the eruption of the Gombe Stratoid Series coincides with a broad stretching event in the region, supporting a model whereby the Gombe Stratoid Series magmatism can be explained by a punctuated phase of rifting that resulted in plate stretching in the Turkana Depression.

Following the Gombe Stratoid Series, basaltic activity in the Turkana Depression takes the form of shield volcanoes. These edifices are located south of the Gombe Plateau, on the eastern shores of Lake Turkana (Figure 2), indicating that magmatism migrated from the volcanically and tectonically active regions (e.g., KSFB/Gombe Plateau) to the shores of the lake. The observation of a migration towards the lake is in agreement with the findings of Vetel and LeGall (2006), whose work suggests that the Kulal and Asie shield volcanoes are part of a magmatic axis that formed in Northern Suguta in the Plio-Pleistocene. In addition, a shift of rifting towards the South Turkana basin that occurred by ca. 2 Ma, and suggested by several authors to have resulted from the northwards propagation of the Kenya Rift (see Muirhead et al., 2022 and references therein; Figure 2), coincides with the migration of magmatic activity. Migration of rifting towards the South Turkana basin may indicate a change in the extensional regimes, giving way to modern magmatism in Turkana, where magmatic activity is limited to axial volcanic centers within the Lake (e.g., Rooney, 2020a; Muirhead et al., 2022). Two main characteristics of the shield volcanoes that followed the Gombe Stratoid Series but preceded this modern axial magmatism are worth noting. First, the volcanic activity of the shields is less voluminous than the Gombe Stratoid Series; this volume difference indicates a less efficient magma plumbing system than Gombe, resulting in primitive compositions and heterogeneity. Second, as magmatism migrates towards Lake Turkana, compositional differences between

the shields and Gombe are noted. Although Type III magmas are evident in both the Gombe Stratoid Series and the shield volcanoes – suggesting a continuity in the sources contributing to magmatism in the region – the latter also begin to exhibit other signatures that are representative of another magma type (e.g., Type IV in Asie and Longipi shields, see following section) and are not found in the Gombe Stratoid Series. Other signatures present in the shield volcanoes, but lacking in the Gombe Stratoid Series, are the negative Zr-Hf anomalies seen in Balo, Lenderit, and Kankam. An important observation is that these signatures are similar to those exhibited by the modern axial volcanic centers in Lake Turkana (e.g., Rooney et al., 2022). Thus, we observe migration of both rifting and magmatism in Turkana, as well as compositional changes in the less voluminous/widespread magmatic events as they migrate. Based on these observations, two questions remain: What is the cause of the compositional changes in the lavas that have erupted in the Turkana Depression? How is the migration of rifting related to the magmatic migration and compositional changes exhibited in these events? We explore the possible causes and the relationship to rifting activity below.

5.3.1 Magma Types in the Turkana Depression - implications on rifting activity

Several magma types have been identified within the EARS on the basis of their geochemical signatures, reflecting different modes of magma generation and source (e.g., Rooney, 2020d). Of particular interest are the Type II, Type III, and Type IV magmas, as these have been present at different stages of rifting within the EARS and in Turkana (see Rooney, 2020d), providing constraints on how melt is generated as rifting progresses. According to Rooney (2020d), Type II magmas commonly occur during incipient lithospheric destabilization; in Turkana, this magma type has been identified in different magmatic events in the Eocene and Miocene (see Rooney, 2017, 2020a). Type II magmas have been suggested by Beccaluva et al. (2009) and Rooney et al. (2014, 2017) to form by destabilization of metasomes in the lithospheric mantle, although other mechanisms have been proposed (see Rooney, 2020d and references therein). Type III magmas are ubiquitous in mature rift sectors within the eastern branch of the EARS (Rooney, 2020d), and have been identified in Turkana throughout the Miocene, Pliocene (this study), and in modern axial magmatism (e.g., Rooney, 2020a; Rooney et al., 2022). This magma type is suggested to

be derived from the asthenosphere and considered to be a mixture of detached African lithosphere, plume material, and depleted mantle (Rooney 2017, 2020d; Rooney et al., 2012b). In contrast, Type IV magmas are the result of mixing between a sublithospheric-derived magma (Type III) and a lithospheric mantle derived lava (Type II) and are typically observed as a rift evolves from its incipient phase (see Rooney, 2020d). This signature has been identified in the modern axial magmatic activity (Rooney, 2020a; Rooney et al., 2022), and as shown in this study, it is also exhibited by some of the Pliocene shield volcanoes.

The geochemical signatures exhibited by the shield volcanoes that deviate from the Type III magma pattern are significant in the context of rifting and magmatism within Turkana. The main deviations identified in the shield volcanoes include the presence of a Type IV magma pattern and the Zr-Hf anomalies in magmas with Type III patterns. As previously discussed, Type IV magmas are a hybrid between Type II and Type III, indicating that both lithospheric and sub-lithospheric sources are contributing to the melt (e.g., Rooney 2020d). Because Type II patterns may involve destabilization of lithospheric metasomes (e.g., Beccaluva et al., 2009; Rooney et al., 2014, 2017), this implies that there must be zones of enriched lithosphere (i.e., metasomes) in Turkana in order to produce Type IV magma signatures. An enrichment of the lithospheric mantle is also in agreement with the Zr-Hf anomalies in Type III patterns that have been identified in the Kankam, Lenderit, and Balo basalts. Such anomalies have been previously attributed to apatite in metasomatic sources (e.g., Rooney, 2020a; Rooney, 2020b and references therein), thus indicating that this mineral phase is present in one of the sources that contributes to these magmas. It is also important to highlight that in Turkana these signatures (e.g., Type IV and Zr-Hf anomalies) are also identified within modern (axial) volcanic centers within Lake Turkana (Rooney, 2020a; Rooney et al., 2022). Moreover, with the exception of Kulal, the Type IV signature of the Pliocene shield volcanoes is only identified in the edifices that are located on the eastern shore of the lake (i.e., Longipi and Asie shield; see Figures 2 and 3). Based on these observations, we propose that enrichments in the lithospheric mantle are present within the Lake Turkana region of the Turkana Depression, as evidenced by Type IV magmas and apatite-influenced anomalies in the relatively recent volcanic activity (i.e., Pliocene shield volcanoes and axial magmatism). Whether this enrichment is due to ancient metasomes (i.e., Pan-African in age; see Rooney et al., 2014) or

modern metasomes formed by previous flood basalt events (e.g., Beccaluva et al., 2009; Rooney, 2020a) is unknown, requiring future isotopic work to properly constrain these enrichments.

Metasomatic signatures in the relatively recent magmas erupted in Turkana may provide insights as to why the modern axial phase behaves differently in this region than in Afar, despite both being of similar magnitude and age (see Rooney 2020a, 2020c). In Turkana, axial magmatism did not erupt over the previously widespread Gombe Stratoid Series; instead, this activity is focused within the Lake Turkana basins (e.g., Rooney, 2020a; Muirhead et al., 2022; Rooney et al., 2022). The migration of rifting towards the South Turkana basin ca. 2 Ma (see Muirhead et al., 2022 and references therein) coincides with the appearance of magma types influenced by metasomatic sources. Furthermore, in the Pliocene shield volcanoes, these signatures are only seen in the volcanic edifices and basaltic units that are located near the eastern shore of the lake (i.e., Longipi and Asie shields, Kankam, Lenderit, and Balo basalts). This suggests that enrichment of the lithosphere may have influenced the migration of rifting in the Turkana Depression. This observation is in agreement with previous rifting models (e.g., Buck 2004) in which regions of enriched lithosphere can generate melts. Consequently, these melts create zones of weaknesses in the lithospheric mantle that can accommodate strain, resulting in zones of focused intrusion within a rift (Buck, 2004). Thus, we hypothesize that magmatism and rifting in the Turkana Depression migrated towards a region with metasomes (i.e., near Lake Turkana), whereby the melting of these lithospheric enrichments resulted in the current focusing of strain.

6. Conclusions

Within the active East African Rift System, the Turkana region has been recognized as the locus of strain (e.g., Rooney, 2020a). In this locality, we focus on the widespread Gombe Stratoid Series and subsequent shield volcanism marks the recommencement of volcanic activity in the Turkana Depression after a period of magmatic quiescence. Similarities between the Gombe Stratoid Series and previous flood basalt volcanism within the EARS are evident, however, these occur at a much smaller scale in Gombe. We suggest that the similarities in characteristics between continental flood basalt systems and the Gombe Stratoid Series may be explained by a relatively high, and sustained flux of asthenosphere-derived magmas into the continental lithosphere. The waning of magma flux results in the subsequent development of shield volcanoes. We further posit that the vast difference in scale between continental flood basalts and the Gombe Stratoid Series reflects differences in the mechanism of melt generation. In East Africa, the Cenozoic flood basalts are widely distributed and were formed by the broad decompression of a plume-sized region of mantle with elevated mantle potential temperature (Rooney 2017; Rooney et al., 2012b). Since the Miocene, magmatism in East Africa has become more focused on the evolving rift, highlighting the role of lithospheric thinning in facilitating decompression of the asthenosphere and the creation of basaltic magmas. Given the asynchronous timing and spatial limitations in episodes of lithospheric thinning throughout East Africa since the Miocene (e.g., Purcell 2018; Macgregor 2015), it is unsurprising magma formation has abated since the early flood basalts. However, the magmas necessary to create the Gombe Stratoid Series required a significant extensional event. We also find that although there is continuity in sources contributing to the Gombe Stratoid Series and the subsequent shield volcanoes of the Stratoid Phase, the movement of magmatism of the shield volcanoes towards an area closer to Lake Turkana results in compositional differences that represent contributions from enriched regions in the lithosphere (Figure 15). The presence of such regions in Turkana may explain the migration of magmatism and rifting towards the lake, where melting of metasomatic sources allows for the focusing of strain and gives way to the modern axial activity within Turkana.

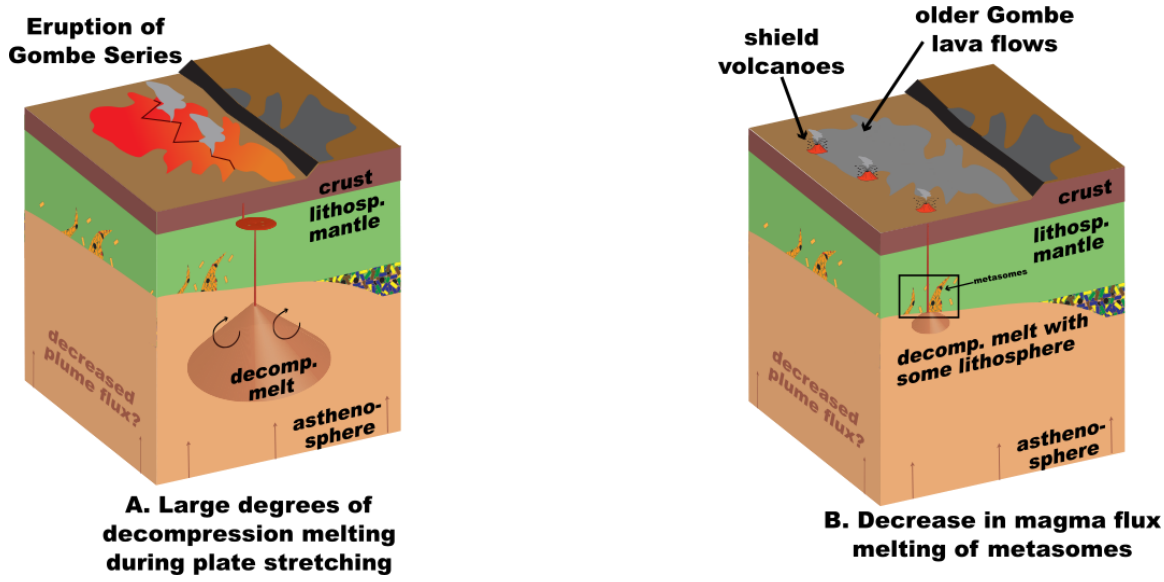

Figure 15. Block model representing the magmatic events of the Stratoid Phase in Turkana. (A) Eruption of the Gombe Stratoid Series as a result of large degrees of decompression melting of the upper mantle during a broad stretching event. The compositional homogeneity of this group indicates that these were differentiated in a complex magma plumbing system. Type III magma signatures exhibited by the Gombe Groups suggest that the melts that generated this high flux event originated in the sub-lithospheric mantle (i.e., asthenosphere). (B) Continuation of basaltic activity in the form of shield volcanoes subsequent to the Gombe eruption. These volcanic edifices are emplaced on top of old Gombe lava flows and are less voluminous. The difference in volume suggests a decrease in the magma flux and a less efficient magma plumbing system than the Gombe Stratoid Series. Despite these differences, there is a continuity in the sources contributing to the melts that generated Gombe as well as the shields, as evidenced by the presence of Type III magma patterns in both volcanic events. However, we note a migration of magmatism towards Lake Turkana and contributions of metasomes in the shield volcanoes, resulting in compositional differences such as Type IV magma patterns and Zr-Hf anomalies. Migration of magmatism and rifting towards zones of lithospheric enrichments allows for the transition to modern axial volcanism, as melting of these metasomes results in the accommodation and focusing of strain in the axial regions of the Turkana basin.

REFERENCES

Abu El-Rus, M. M. A., & Rooney, T. O. (2017). Insights into the lithosphere to asthenosphere melting transition in northeast Africa: Evidence from the Tertiary volcanism in middle Egypt. *Chemical Geology*, *455*, 282–303. https://doi.org/10.1016/j.chemgeo.2016.10.005

Asfaw, B., Beyene, Y., Semaw, S., Suwa, G., White, T., & WoldeGabriel, G. (1991). Fejej: a new paleoanthropological research area in Ethiopia. *Journal of Human Evolution*, *21*(2), 137–143. https://doi.org/10.1016/0047-2484(91)90004-F

Ayalew, D., Barbey, P., Marty, B., Reisberg, L., Yirgu, G., & Pik, R. (2002). Source, genesis, and timing of giant ignimbrite deposits associated with Ethiopian continental flood basalts. *Geochimica et Cosmochimica Acta*, *66*(8), 1429–1448. https://doi.org/10.1016/S0016-7037(01)00834-1

Beccaluva, L., Bianchini, G., Natali, C., & Siena, F. (2009). Continental Flood Basalts and Mantle Plumes: a Case Study of the Northern Ethiopian Plateau. *Journal of Petrology*, *50*(7), 1377–1403. https://doi.org/10.1093/petrology/egp024

Bohrson, W. A., Spera, F. J., Ghiorso, M. S., Brown, G. A., Creamer, J. B., & Mayfield, A. (2014). Thermodynamic Model for Energy-Constrained Open-System Evolution of Crustal Magma Bodies Undergoing Simultaneous Recharge, Assimilation and Crystallization: the Magma Chamber Simulator. *Journal of Petrology*, *55*(9), 1685–1717. https://doi.org/10.1093/petrology/egu036

Bonini, M., Corti, G., Innocenti, F., Manetti, P., Mazzarini, F., Abebe, T., & Pecskay, Z. (2005). Evolution of the Main Ethiopian Rift in the frame of Afar and Kenya rifts propagation. Tectonics, 24(1). https://doi.org/10.1029/2004TC001680

Boschetto, H. B., Brown, F. H., & McDougall, I. (1992). Stratigraphy of the Lothidok Range, northern Kenya, andK/Ar ages of its Miocene primates. *Journal of Human Evolution*, *22*(1), 47–71. https://doi.org/10.1016/0047-2484(92)90029-9

Bosworth, W. (1992). Mesozoic and early Tertiary rift tectonics in East Africa. Tectonophysics, 209(1–4), 115–137. https://doi.org/10.1016/0040-1951(92)90014-W

Bridges, D. L., Mickus, K., Gao, S. S., Abdelsalam, M. G., & Alemu, A. (2012). Magnetic stripes of a transitional continental rift in Afar. *Geology*, *40*(3), 203–206. https://doi.org/10.1130/G32697.1

Brown, E. L., Rooney, T. O., Moucha, R., Stein, S., & Stein, C. A. (2022). Temporal evolution of mantle temperature and lithospheric thickness beneath the ~1.1 Ga Midcontinent Rift, North America: Implications for rapid motion of Laurentia. *Earth and Planetary Science Letters*, *598*, 117848. https://doi.org/10.1016/j.epsl.2022.117848

Brown, F. H., & McDougall, I. (2011). Geochronology of the Turkana Depression of Northern Kenya and Southern Ethiopia. *Evolutionary Anthropology: Issues, News, and Reviews*, *20*(6), 217–227. https://doi.org/10.1002/evan.20318

Bruhn, R. L., Brown, F. H., Gathogo, P. N., & Haileab, B. (2011). Pliocene volcano-tectonics and paleogeography of the Turkana Basin, Kenya and Ethiopia. *Journal of African Earth Sciences*, *59*(2–3), 295–312. https://doi.org/10.1016/j.jafrearsci.2010.12.002

Bryan, W. B. (1979). Regional Variation and Petrogenesis of Basalt Glasses from the FAMOUS Area, Mid-

Atlantic Ridge. *Journal of Petrology*, *20*(2), 293–325. https://doi.org/10.1093/petrology/20.2.293

Buck, W. R. (2004). Consequences of Asthenospheric Variability on Continental Rifting. In G. Karner, B. Taylor, N. W. Driscoll, & D. L. Kohlstedt (Eds.), *Rheology and Deformation of the Lithosphere at Continental Margins* (pp. 1–30). Columbia University Press. https://doi.org/10.7312/karn12738-002

Chiasera, B., Rooney, T. O., Bastow, I. D., Yirgu, G., Grosfils, E. B., Ayalew, D., et al. (2021). Magmatic rifting in the Main Ethiopian Rift began in thick continental lithosphere; the case of the Galema Range. *Lithos*, *406–407*, 106494. https://doi.org/10.1016/j.lithos.2021.106494

Chorowicz, J. (2005). The East African rift system. *Journal of African Earth Sciences*, 32.
Corti, G. (2009). Continental rift evolution: From rift initiation to incipient break-up in the Main Ethiopian Rift, East Africa. *Earth-Science Reviews*, *96*(1), 1–53. https://doi.org/10.1016/j.earscirev.2009.06.005

Cox, K. G. (1980). A Model for Flood Basalt Vulcanism. *Journal of Petrology*, *21*(4), 629–650. https://doi.org/10.1093/petrology/21.4.629

Danyushevsky, L. V., & Plechov, P. (2011). Petrolog3: Integrated software for modeling crystallization processes. *Geochemistry, Geophysics, Geosystems*, *12*(7). https://doi.org/10.1029/2011GC003516

Davis, W. R., Collins, M. A., Rooney, T. O., Brown, E. L., Stein, C. A., Stein, S., & Moucha, R. (2022). Geochemical, petrographic, and stratigraphic analyses of the Portage Lake Volcanics of the Keweenawan CFBP: implications for the evolution of main stage volcanism in continental flood basalt provinces. *Geological Society, London, Special Publications*, *518*(1), 67–100. https://doi.org/10.1144/SP518-2020-221

Dunkley, P. N., Smith, M., Allen, D. J., & Darling, W. G. (1993). *The geothermal activity and geology of the northern sector of the Kenya Rift Valley* (p. 202). Nottingham, UK: British Geological Survey. Retrieved from http://nora.nerc.ac.uk/id/eprint/507920/

Dunn, T. (1987). Partitioning of Hf, Lu, Ti, and Mn between olivine, clinopyroxene and basaltic liquid. *Contributions to Mineralogy and Petrology*, *96*(4), 476–484. https://doi.org/10.1007/BF01166692

Ebinger, C. (2005). Continental break-up: The East African perspective. *Astronomy and Geophysics*, *46*(2), 2.16-2.21. https://doi.org/10.1111/j.1468-4004.2005.46216.x

Ebinger, C. J., & Ibrahim, A. (1994). Multiple episodes of rifting in Central and East Africa: A re-evaluation of gravity data. *Geologische Rundschau*, *83*(4), 689–702. https://doi.org/10.1007/BF00251068

Ebinger, C. J., Yemane, T., Woldegabriel, G., Aronson, J. L., & Walter, R. C. (1993). Late Eocene–Recent volcanism and faulting in the southern main Ethiopian rift. *Journal of the Geological Society*, *150*(1), 99–108. https://doi.org/10.1144/gsjgs.150.1.0099

Ebinger, C J, Yemane, T., Kelley, S., & Rex, D. C. (2000). Rift deflection, migration, and propagation: Linkage of the Ethiopian and Eastern rifts, Africa. *Geological Society of America Bulletin*, *112*(2), 14.

Ebinger, Cynthia J., van Wijk, J., & Keir, D. (2013). The time scales of continental rifting: Implications for global processes. In M. E. Bickford, *The Web of Geological Sciences: Advances, Impacts, and Interactions*. Geological Society of America. https://doi.org/10.1130/2013.2500(11)

Feibel, C. S. (2011). A Geological History of the Turkana Basin. *Evolutionary Anthropology: Issues, News,*

and Reviews, *20*(6), 206–216. https://doi.org/10.1002/evan.20331

Ferguson, D. J., Calvert, A. T., Pyle, D. M., Blundy, J. D., Yirgu, G., & Wright, T. J. (2013). Constraining timescales of focused magmatic accretion and extension in the Afar crust using lava geochronology. *Nature Communications*, *4*(1), 1416. https://doi.org/10.1038/ncomms2410

Furman, T., Kaleta, K. M., Bryce, J. G., & Hanan, B. B. (2006). Tertiary Mafic Lavas of Turkana, Kenya: Constraints on East African Plume Structure and the Occurrence of High-μ Volcanism in Africa. *Journal of Petrology*, *47*(6), 1221–1244. https://doi.org/10.1093/petrology/egl009

Gathogo, P. N., Brown, F. H., & McDougall, I. (2008). Stratigraphy of the Koobi Fora Formation (Pliocene and Pleistocene) in the Loiyangalani region of northern Kenya. *Journal of African Earth Sciences*, *51*(5), 277–297. https://doi.org/10.1016/j.jafrearsci.2008.01.010

Gualda, G. A. R., Ghiorso, M. S., Lemons, R. V., & Carley, T. L. (2012). Rhyolite-MELTS: a Modified Calibration of MELTS Optimized for Silica-rich, Fluid-bearing Magmatic Systems. *Journal of Petrology*, *53*(5), 875–890. https://doi.org/10.1093/petrology/egr080

Haileab, B., Brown, F. H., McDougall, I., & Gathogo, P. N. (2004). Gombe Group basalts and initiation of Pliocene deposition in the Turkana depression, northern Kenya and southern Ethiopia. *Geological Magazine*, *141*(1), 41–53. https://doi.org/10.1017/S001675680300815X

Hendrie, D. B., Kusznir, N. J., Morley, C. K., & Ebinger, C. J. (1994). Cenozoic extension in northern Kenya: a quantitative model of rift basin development in the Turkana region. *Tectonophysics*, *236*(1), 409–438. https://doi.org/10.1016/0040-1951(94)90187-2

Higuchi, H., & Nagasawa, H. (1969). Partition of trace elements between rock-forming minerals and the host volcanic rocks. *Earth and Planetary Science Letters*, *7*(3), 281–287. https://doi.org/10.1016/0012-821X(69)90066-1

Humphreys, M. C. S., Edmonds, M., Plail, M., Barclay, J., Parkes, D., & Christopher, T. (2013). A new method to quantify the real supply of mafic components to a hybrid andesite. *Contributions to Mineralogy and Petrology*, *165*(1), 191–215. https://doi.org/10.1007/s00410-012-0805-x

Keir, D. (2014). Magmatism and deformation during continental breakup. *Astronomy & Geophysics*, *55*(5), 5.18-5.22. https://doi.org/10.1093/astrogeo/atu213

Keir, D., Bastow, I. D., Pagli, C., & Chambers, E. L. (2013). The development of extension and magmatism in the Red Sea rift of Afar. *Tectonophysics*, *607*, 98–114. https://doi.org/10.1016/j.tecto.2012.10.015

Key, R. M., Rop, B. P., & Rundle, C. C. (1987). The development of the Late Cenozoic alkali basaltic Marsabit Shield Volcano, northern Kenya. *Journal of African Earth Sciences (1983)*, *6*(4), 475–491. https://doi.org/10.1016/0899-5362(87)90089-3

Key, R.M.,Watkins, R.T., 1988. Geology of the Sabarei area. Republic of Kenya Ministry of Environment and Natural Resources, Mines and Geological Department Report. 111.

Kieffer, B., Arndt, N., Lapierre, H., Bastien, F., Bosch, D., Pecher, A., et al. (2004). Flood and Shield Basalts from Ethiopia: Magmas from the African Superswell. *Journal of Petrology*, *45*(4), 793–834. https://doi.org/10.1093/petrology/egg112

Kimura, J.-I., & Kawabata, H. (2014). Trace element mass balance in hydrous adiabatic mantle melting:

The Hydrous Adiabatic Mantle Melting Simulator version 1 (HAMMS1). *Geochemistry, Geophysics, Geosystems*, *15*(6), 2467–2493. https://doi.org/10.1002/2014GC005333

Krans, S. R., Rooney, T. O., Kappelman, J., Yirgu, G., & Ayalew, D. (2018). From initiation to termination: a petrostratigraphic tour of the Ethiopian Low-Ti Flood Basalt Province. *Contributions to Mineralogy and Petrology*, *173*(5), 37. https://doi.org/10.1007/s00410-018-1460-7

Lee, C.-T. A., Luffi, P., Plank, T., Dalton, H., & Leeman, W. P. (2009). Constraints on the depths and temperatures of basaltic magma generation on Earth and other terrestrial planets using new thermobarometers for mafic magmas. *Earth and Planetary Science Letters*, *279*(1–2), 20–33. https://doi.org/10.1016/j.epsl.2008.12.020

Lee, C.-T. A., Lee, T. C., & Wu, C.-T. (2014). Modeling the compositional evolution of recharging, evacuating, and fractionating (REFC) magma chambers: Implications for differentiation of arc magmas. *Geochimica et Cosmochimica Acta*, *143*, 8–22. https://doi.org/10.1016/j.gca.2013.08.009

Macgregor, D. (2015). History of the development of the East African Rift System: A series of interpreted maps through time. *Journal of African Earth Sciences*, *101*, 232–252. https://doi.org/10.1016/j.jafrearsci.2014.09.016

McDougall, Ian, & Brown, F. H. (2008). Geochronology of the pre-KBS Tuff sequence, Omo Group, Turkana Basin. *Journal of the Geological Society*, *165*(2), 549–562. https://doi.org/10.1144/0016-76492006-170

McDougall, Ian, & Brown, F. H. (2009). Timing of volcanism and evolution of the northern Kenya Rift. *Geological Magazine*, *146*(1), 34–47. https://doi.org/10.1017/S0016756808005347

McDougall, IAN, & Feibel, C. S. (1999). Numerical age control for the Miocene-Pliocene succession at Lothagam, a hominoid-bearing sequence in the northern Kenya Rift. *Journal of the Geological Society*, *156*, 15.

Merle, O. (2011). A simple continental rift classification. *Tectonophysics*, *513*(1), 88–95. https://doi.org/10.1016/j.tecto.2011.10.004

Morley, C. K., Wescott, W. A., Stone, D. M., Harper, R. M., Wigger, S. T., & Karanja, F. M. (1992). Tectonic evolution of the northern Kenyan Rift. *Journal of the Geological Society*, *149*(3), 333–348. https://doi.org/10.1144/gsjgs.149.3.0333

Muirhead, J. D., Kattenhorn, S. A., Lee, H., Mana, S., Turrin, B. D., Fischer, T. P., et al. (2016). Evolution of upper crustal faulting assisted by magmatic volatile release during early-stage continental rift development in the East African Rift. *Geosphere*, *12*(6), 1670–1700. https://doi.org/10.1130/GES01375.1

Ochieng, J.O.,Wilkinson, A.F., 1988. Geology of the Loiyangalani Area: Degree: Ministry of Environment and Natural Resources. Ministry of Environment, and Natural Resources, Kenya.

O'Hara, M. J., & Mathews, R. E. (1981). Geochemical evolution in an advancing, periodically replenished, periodically tapped, continuously fractionated magma chamber. Journal of the Geological Society, 138(3), 237–277. https://doi.org/10.1144/gsjgs.138.3.0237

O'Hara, M. J., & Mathews, R. E. (1981). Geochemical evolution in an advancing, periodically replenished, periodically tapped, continuously fractionated magma chamber. *Journal of the Geological Society*, *138*(3),

237–277. https://doi.org/10.1144/gsjgs.138.3.0237

Opdyke, N. D., Kent, D. V., Huang, K., Foster, D. A., & Patel, J. P. (2010). Equatorial paleomagnetic time-averaged field results from 0-5 Ma lavas from Kenya and the latitudinal variation of angular dispersion: PALEOMAGNETISM OF PLIOCENE-PLEISTOCENE KENYA LAVAS. *Geochemistry, Geophysics, Geosystems*, *11*(5), n/a-n/a. https://doi.org/10.1029/2009GC002863

Purcell, P. G. (2018). Re-imagining and re-imaging the development of the East African Rift. *Petroleum Geoscience*, *24*(1), 21–40. https://doi.org/10.1144/petgeo2017-036

Putirka, K. (2016). Special Collection: Olivine: Rates and styles of planetary cooling on Earth, Moon, Mars, and Vesta, using new models for oxygen fugacity, ferric-ferrous ratios, olivine-liquid Fe-Mg exchange, and mantle potential temperature. *American Mineralogist*, *101*(4), 819–840. https://doi.org/10.2138/am-2016-5402

Rollinson, H. R. (1993). *Using geochemical data: evaluation, presentation, interpretation*. Harlow, Essex, England : New York: Longman Scientific & Technical ; Copublished in the U.S. with J. Wiley & Sons.

Rooney, T. O. (2017). The Cenozoic magmatism of East-Africa: Part I — Flood basalts and pulsed magmatism. *Lithos*, *286–287*, 264–301. https://doi.org/10.1016/j.lithos.2017.05.014

Rooney, T. O. (2020a). The Cenozoic magmatism of East Africa: Part II – Rifting of the mobile belt. *Lithos*, *360–361*, 105291. https://doi.org/10.1016/j.lithos.2019.105291

Rooney, T. O. (2020b). The Cenozoic magmatism of East Africa: Part III – Rifting of the craton. *Lithos*, *360–361*, 105390. https://doi.org/10.1016/j.lithos.2020.105390

Rooney, T. O. (2020c). The Cenozoic magmatism of East Africa: Part IV – The terminal stages of rifting preserved in the Northern East African Rift System. *Lithos*, *360–361*, 105381. https://doi.org/10.1016/j.lithos.2020.105381

Rooney, T. O. (2020d). The Cenozoic magmatism of East Africa: Part V – Magma sources and processes in the East African Rift. *Lithos*, *360–361*, 105296. https://doi.org/10.1016/j.lithos.2019.105296

Rooney, T. O., Herzberg, C., & Bastow, I. D. (2012). Elevated mantle temperature beneath East Africa. *Geology*, *40*(1), 27–30. https://doi.org/10.1130/G32382.1

Rooney, T. O., Hart, W. K., Hall, C. M., Ayalew, D., Ghiorso, M. S., Hidalgo, P., & Yirgu, G. (2012). Peralkaline magma evolution and the tephra record in the Ethiopian Rift. *Contributions to Mineralogy and Petrology*, *164*(3), 407–426. https://doi.org/10.1007/s00410-012-0744-6

Rooney, T. O., Hanan, B. B., Graham, D. W., Furman, T., Blichert-Toft, J., & Schilling, J.-G. (2012). Upper Mantle Pollution during Afar Plume–Continental Rift Interaction. *Journal of Petrology*, *53*(2), 365–389. https://doi.org/10.1093/petrology/egr065

Rooney, T. O., Nelson, W. R., Dosso, L., Furman, T., & Hanan, B. (2014). The role of continental lithosphere metasomes in the production of HIMU-like magmatism on the northeast African and Arabian plates. *Geology*, *42*(5), 419–422. https://doi.org/10.1130/G35216.1

Rooney, T. O., Nelson, W. R., Ayalew, D., Hanan, B., Yirgu, G., & Kappelman, J. (2017). Melting the lithosphere: Metasomes as a source for mantle-derived magmas. *Earth and Planetary Science Letters*, *461*,

105–118. https://doi.org/10.1016/j.epsl.2016.12.010

Rooney, T. O., Wallace, P. J., Muirhead, J. D., Chiasera, B., Steiner, R. A., Girard, G., & Karson, J. A. (2022). Transition to magma-driven rifting in the South Turkana Basin, Kenya: Part 2. *Journal of the Geological Society*, *179*(6), jgs2021-160. https://doi.org/10.1144/jgs2021-160

Rowan, C. M. (2021). *40Ar/39Ar geochronology of the Lothagam Basalt, Turkana Depression, Kenya*. Rutgers University - School of Graduate Studies. https://doi.org/10.7282/t3-3fey-8k58

Schneider, C. A., Rasband, W. S., & Eliceiri, K. W. (2012). NIH Image to ImageJ: 25 years of image analysis. *Nature Methods*, *9*(7), 671–675. https://doi.org/10.1038/nmeth.2089

Scholz, C. H., & Contreras, J. C. (1998). Mechanics of continental rift architecture. *Geology*, *26*(11), 967–970. https://doi.org/10.1130/0091-7613(1998)026<0967:MOCRA>2.3.CO;2

Shillington, D. J., Scott, C. L., Minshull, T. A., Edwards, R. A., Brown, P. J., & White, N. (2009). Abrupt transition from magma-starved to magma-rich rifting in the eastern Black Sea. *Geology*, *37*(1), 7–10. https://doi.org/10.1130/G25302A.1

Steiner, R. A., & Rooney, T. O. (2021). PiAutoStage: An Open-Source 3D Printed Tool for the Automatic Collection of High-Resolution Microscope Imagery. *Geochemistry, Geophysics, Geosystems*, *22*(5), e2021GC009693. https://doi.org/10.1029/2021GC009693

Steiner, R. A., Rooney, T. O., Girard, G., Rogers, N., Ebinger, C. J., Peterson, L., & Phillips, R. K. (2022). Initial Cenozoic magmatic activity in East Africa: new geochemical constraints on magma distribution within the Eocene continental flood basalt province. *Geological Society, London, Special Publications*, *518*(1), 435–465. https://doi.org/10.1144/SP518-2020-262

Sun, C., Graff, M., & Liang, Y. (2017). Trace element partitioning between plagioclase and silicate melt: The importance of temperature and plagioclase composition, with implications for terrestrial and lunar magmatism. *Geochimica et Cosmochimica Acta*, *206*, 273–295. https://doi.org/10.1016/j.gca.2017.03.003

Sun, S. -s., & McDonough, W. F. (1989). Chemical and isotopic systematics of oceanic basalts: implications for mantle composition and processes. *Geological Society, London, Special Publications*, *42*(1), 313–345. https://doi.org/10.1144/GSL.SP.1989.042.01.19

Thy, P. (1983). Phase relations in transitional and alkali basaltic glasses from Iceland. *Contributions to Mineralogy and Petrology*, *82*(2), 232–251. https://doi.org/10.1007/BF01166618

Vetel, W., & Le Gall, B. (2006). Dynamics of prolonged continental extension in magmatic rifts: the Turkana Rift case study (North Kenya). *Geological Society, London, Special Publications*, *259*(1), 209–233. https://doi.org/10.1144/GSL.SP.2006.259.01.17

Vetel, W., Le Gall, B., & Walsh, J. J. (2005). Geometry and growth of an inner rift fault pattern: the Kino Sogo Fault Belt, Turkana Rift (North Kenya). *Journal of Structural Geology*, *27*(12), 2204–2222. https://doi.org/10.1016/j.jsg.2005.07.003

Villiger, S., Ulmer, P., Müntener, O., & Thompson, A. B. (2004). The Liquid Line of Descent of Anhydrous, Mantle-Derived, Tholeiitic Liquids by Fractional and Equilibrium Crystallization—an Experimental Study at 1·0 GPa. *Journal of Petrology*, *45*(12), 2369–2388. https://doi.org/10.1093/petrology/egh042

Watkins, R. T. (1986). Volcano-tectonic control on sedimentation in the Koobi Fora sedimentary basin, Lake Turkana. *Geological Society, London, Special Publications*, *25*(1), 85–95. https://doi.org/10.1144/GSL.SP.1986.025.01.08